Directional semivariogram analysis to identify and rank controls on the spatial variability of fracture networks

John R. Hanke, Mark P. Fischer[*], Ryan M. Pollyea[1]

Department of Geology and Environmental Geosciences, Northern Illinois University, DeKalb, IL 60115-2828, USA

ARTICLE INFO

ABSTRACT

In this study, the directional semivariogram is deployed to investigate the spatial variability of map-scale fracture network attributes in the Paradox Basin, Utah. The relative variability ratio (R) is introduced as the ratio of integrated anisotropic semivariogram models, and R is shown to be an effective metric for quantifying the magnitude of spatial variability for any two azimuthal directions. R is applied to a GIS-based data set comprising roughly 1200 fractures, in an area which is bounded by a map-scale anticline and a km-scale normal fault. This analysis reveals that proximity to the fault strongly influences the magnitude of spatial variability for both fracture intensity and intersection density within 1–2 km. Additionally, there is significant anisotropy in the spatial variability, which is correlated with trends of the anticline and fault. The direction of minimum spatial correlation is normal to the fault at proximal distances, and gradually rotates and becomes subparallel to the fold axis over the same 1–2 km distance away from the fault. We interpret these changes to reflect varying scales of influence of the fault and the fold on fracture network development: the fault locally influences the magnitude and variability of fracture network attributes, whereas the fold sets the background level and structure of directional variability.

1. Introduction

In geological systems, a homogeneous material comprises uniform attributes over a given spatial domain (e.g., density, porosity, permeability, elastic moduli). Although the properties of natural geological systems are rarely, if ever, homogeneous, the classification of something as such is often useful. For example, spatial homogeneity greatly simplifies mathematical formulations of heat transfer, fluid flow, and linear elasticity (e.g., Pollard and Fletcher, 2005; Fairley, 2016). However, the application of these mathematical models to natural systems requires the qualification that homogeneity is assumed over an appropriate support scale (Rubin, 2003). This support scale is defined on the basis of statistical homogeneity or macroscopic averaging, in which the variability of a material property converges on an expected value over a range of length scales, commonly called the continuum scale (Guéguen and Palciauskas, 1994).

In the field of geostatistics, spatial variability is a concept that describes how measurable attributes vary in the spatial domain (Deutsch, 2002). At a given scale, a perfectly homogeneous system has zero detectable spatial variability, which means the measurable value for a given material property will be the same at all positions within the

domain of interest. By comparison, heterogeneous systems will display some detectable and non-zero amount of spatial variability at a particular scale. Geostatistics provides a set of tools to quantify the attributes of spatial variability, including its structure, magnitude and directional dependence (anisotropy), as well as systematic methods for modeling spatially variable system attributes (Kitanidis, 1997; Deutsch and Journel, 1998; Deutsch, 2002).

A fractured volume of rock is an excellent example of a spatial domain comprising attributes that often display a significant degree of spatial variability. Examples of these attributes include fracture length per unit area, fracture area per unit volume, number of fracture intersections per unit area or volume, and fracture orientation; all of these attributes could vary from place to place throughout a fractured rock mass, and in ways that are imperceptible to the naked eye. Quantitative characterization and analysis of the spatial variability of these and other characteristics of fracture networks has a wide range of industrial applications because fractures reduce the structural integrity of materials, create conduits and barriers that can enhance or impede subsurface fluid flow, and can impact how subsurface data are either collected, interpreted or predicted. In general, quantitative fracture network characterization has traditionally been investigated using 1-D

---

scanline methods; however, recent advances in fracture network data acquisition (e.g., remote sensing, microseismic) have made it possible to examine the spatial attributes of fracture networks on the basis of data-intensive 2- and 3-D geostatistical methods.

1.1. Fracture network characterization using scanlines

Field structural geologists most often characterize fracture networks (Sanderson and Nixon, 2015) using 1-D scanlines that are oriented perpendicular to a fracture set of known orientation, timing, mode, or filling (Watkins et al., 2015). Along a scanline, geologists record the location of each fracture intersecting the scanline, as well as other attributes of interest, such as aperture for joints, throw for faults, or the degree of fracture mineralization. Scanlines are a common method for fracture data collection because they are easily employed on vertical and horizontal outcrop surfaces of limited extent, and because they yield data that are similar to that collected along boreholes.

Many workers have used scanlines to analyze the *statistical distribution* of sampled fracture attributes like height (Bisdom et al., 2014), aperture (e.g., Gudmundsson et al., 2001; André-Mayer and Sausse, 2007; Hooker et al., 2013; Santos et al., 2015), spacing and throw (e.g., Gillespie et al., 1993; Ortega et al., 2006; Putz-Perrier and Sanderson, 2010; Soden et al., 2016). These studies often have one or two aims: (1) to establish mathematical relationships that facilitate the prediction or modeling of fracture attributes, or (2) to elucidate how the processes of fracture initiation, growth, interaction, arrest and mineralization might lead to an observed attribute distribution (e.g., Olson, 2004; Fischer and Polansky, 2006; André-Mayer and Sausse, 2007; Hooker et al., 2013).

To investigate the *spatial distribution* of fractures or fracture attributes, workers typically plot the value or cumulative value of an attribute along a scanline (e.g., Putz-Perrier and Sanderson, 2010; Riley et al., 2010; Hooker et al., 2013; Rotevatn et al., 2013; Sagi et al., 2016), or calculate the coefficient of variation (C_v) for all the attribute values collected along a single scanline (e.g., Gillespie et al., 1999, 2001; André-Mayer and Sausse, 2007; Deng et al., 2013; Hooker and Katz, 2015; Wennberg et al., 2016). Although these approaches are typically used to quantify the degree to which fractures are randomly distributed or clustered along the scanline, they are more accurately described as measures of sample variability, not spatial variability. Recent work by Li et al. (2017) and Marrett et al. (2017) eliminates these shortcomings by using a normalized correlation count method to more precisely assess the manner and degree to which fractures are spatially correlated. Unlike C_v-based approaches, their method *can* assess spatial variability because it incorporates the sequence of fracture spacings along a scanline. To document directional or large-scale variations in fracture attributes, such as those that might occur in kilometer-scale folds or near faults, geologists typically use multiple scanlines of different orientation and/or location (e.g., Berg and Skar, 2005; Laubach et al., 2014; Watkins et al., 2015; Choi et al., 2016; Cilona et al., 2016). These approaches cannot directly characterize the manner in which fracture or fracture network properties change between scanlines or in directions that are not parallel to a scanline.

1.2. Fracture network characterization using geostatistics

While it is convenient to categorize the abundant scanline-based studies of fracture networks as "geostatistics", this term is more appropriately reserved for the suite of spatial statistical tools that are based on the Theory of Regionalized Variables (Matheron, 1963). In this context, Matheron (1963) defined a regionalized variable (RV) as having three primary attributes: (1) the RV is localized such that variations occur over a geometrical space or "support scale"; (2) the RV is

characterized by variable spatial continuity with the extreme case of no spatial continuity defined as the "nugget effect"; and (3) the spatial continuity of a RV may exhibit directionality (i.e., anisotropy). Further discussion of the RV construct is presented in Appendix A.

The concept of spatial continuity is rooted in what is often referred to as the first law of geography, which states that attributes separated by short distances are more related than those separated by long distances (Tobler, 1970; Miller, 2004). In general terms, the presence of spatial continuity implies a degree of spatial correlation. Unfortunately, the terms spatial continuity and correlation are often used synonymously with spatial variability, creating a dangerously misleading equivalence. For example, a RV with non-zero variance exhibits spatial variability; however, the spatial continuity (i.e., spatial correlation) depends on whether or not the value of the RV is dependent on separation distance. As a result, spatial variability can exist in the absence of spatial continuity, whereas the absence of spatial variability (i.e., homogeneity) ensures maximum spatial continuity.

Geostatistics provides a means to describe and quantify the spatial continuity of physical phenomena (Isaaks and Srivastava, 1989) and has been used in fields ranging from geology to meteorology, biology, agriculture and public health. Kriging, sequential simulation, and semivariogram analysis are among the most widely used geostatistical tools, and there are numerous examples of geostatistical analyses of fracture networks (e.g., Gervais et al., 1995; Viruete et al., 2003; Sisavath et al., 2004; Neuman, 2005; Dowd et al., 2007; Rafiee and Vinches, 2008; Dewit et al., 2012; Koike et al., 2015). The concept of spatial anisotropy has proven particularly useful for understanding and modeling fluid flow in fractured geological media. For example, Pollyea and Fairley (2012) invoked geostatistical methods to quantify the anisotropic nature of fracture occurrence in basalt outcrops, and then implemented semivariogram analysis and sequential indicator simulation to develop equally probable, but spatially variable reservoirs for modeling CO_2 sequestration in basalt formations. Similarly, Pollyea et al. (2013) invoked the semivariogram of fracture occurrence to optimize spatial sampling patterns for fractured basalt characterization, and Pollyea and Fairley (2011) implemented semivariogram analysis on LiDAR scans of basalt outcrops to illustrate that discrete fracture networks can be extracted as second-order information from a LiDAR point cloud. In contrast to techniques that rely on scanlines and the coefficient of variation, geostatistical tools like the semivariogram do quantify the spatial continuity and variability of regionalized variables. These tools also enable users to identify trends in spatial continuity, and to recognize the distances over which spatial correlation ends and statistical randomness begins.

In this paper, we use semivariogram analysis to characterize and quantitatively compare the amount and style of variability displayed by a natural fracture network that is exposed in the footwall of a kilometer-scale normal fault that formed in the limb of a map scale anticline. Our aim is to understand the relative role these structures played in controlling the spatial variability of fracture network properties. We specifically focus on the spatial variability of fracture intensity and intersection density as these are proxies for secondary porosity and permeability, and as such, are indicators of the efficiency of fluid storage and flow through fractured rock masses (Rohrbaugh et al., 2002). Determining the magnitude and correlation structure of spatial variability displayed by this fracture network allows us to infer the geological or geomechanical causes of the variability, and provides quantitative information that can be included in predictive, stochastic models of spatially varying fracture, and fracture network properties.

2. Geological background

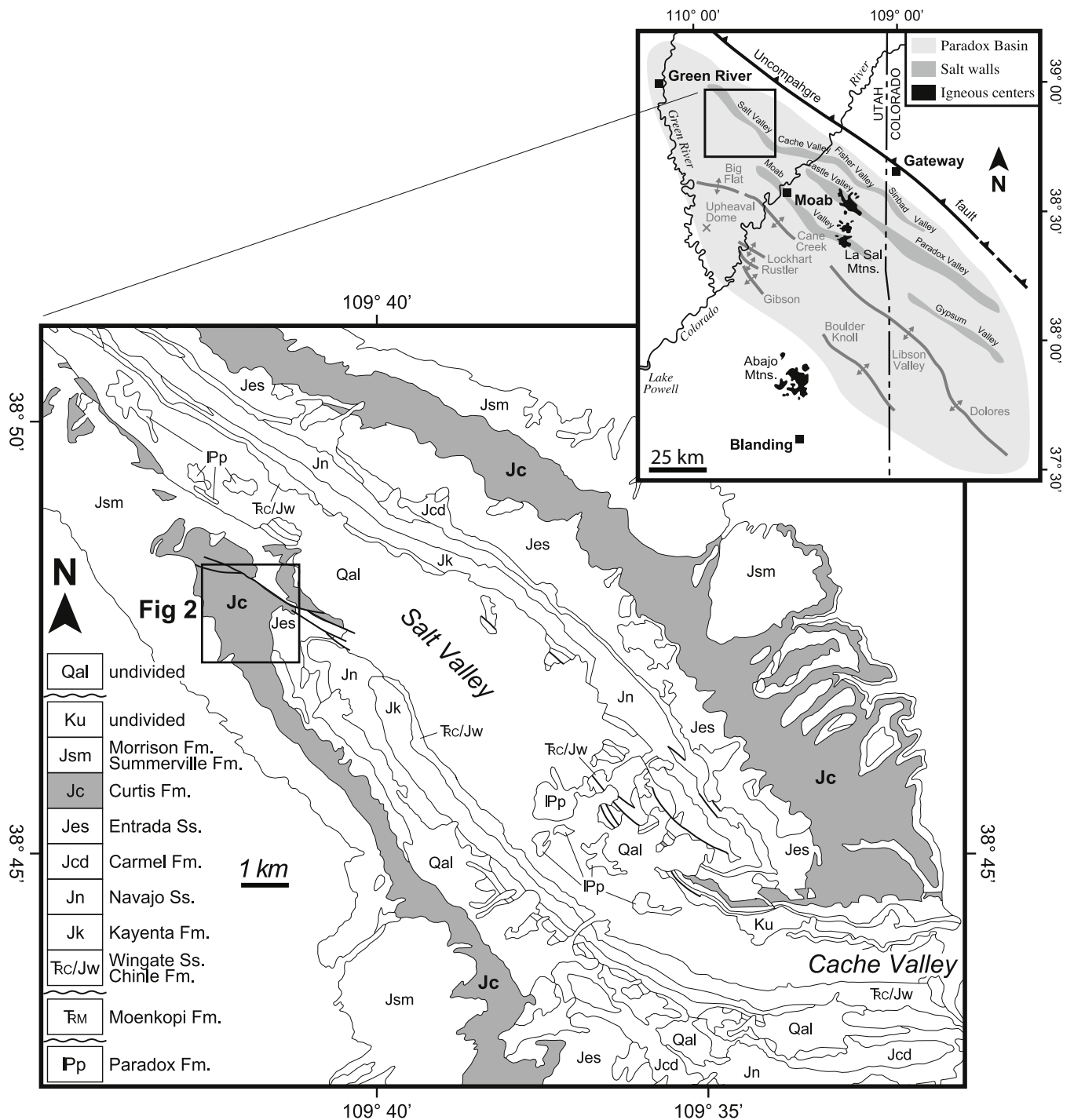We examined the fracture network in a roughly 2.5 km^2 area of

Fig. 1. Simplified geological and location map of Salt Valley anticline. Shaded area highlights well-fractured exposures of the Jurassic Curtis Formation. Modified after Doelling (1985).

nearly complete exposure in the southwestern limb of Salt Valley anticline, near Moab, Utah, U.S.A. (Fig. 1). The anticline is cored by a mixed evaporite, carbonate and shale succession of the Pennsylvanian Paradox Formation, and is one of several NW-SE trending salt walls in the Paradox Basin (Doelling, 1985; Trudgill, 2011). These halokinetic structures are interpreted to have formed when differential loading associated with SW-prograding deposition of late Paleozoic and Meso-zoic sediments induced salt flow and localized diapirism above normal fault-related steps in the Mississippian basement (Doelling et al., 1988;

Huntoon, 1988). Like many of the salt walls throughout the basin, the crest of the anticline is interpreted to have collapsed due to a combi-nation of localized normal faulting and salt dissolution after epeiro-genic uplift exhumed the region, beginning approximately 10 million years ago (Doelling et al., 1988). Our specific study area is located in the Klondike Bluffs region, roughly 5 km northeast of the U.S. Highway 190 entrance to Canyonlands Airport (Fig. 1). In this region the trend of Salt Valley anticline changes from approximately 320°, southeast of the bluffs, to approximately 305°, northwest of the bluffs. Bedding is
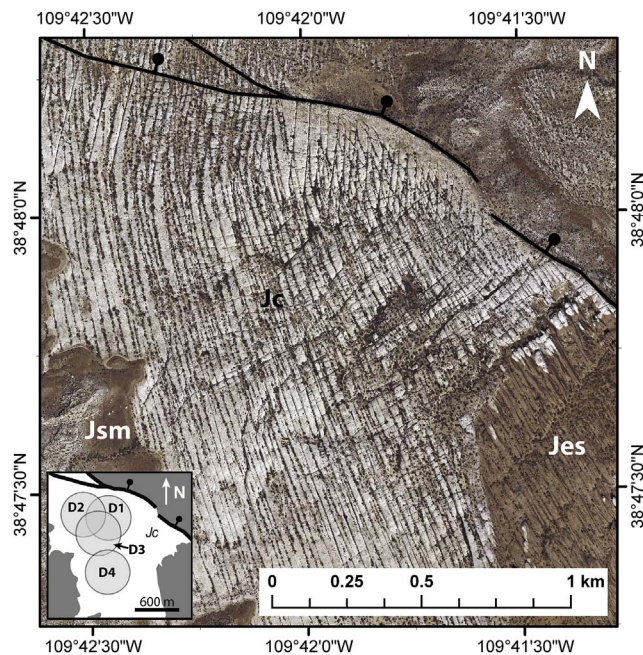
Fig. 2. Aerial image of the Klondike Bluffs region. Light colored outcrops expose the Moab Member of the Curtis Formation, whereas darker, red-brown outcrops expose the Slickrock Member of the Entrada Sandstone. See Fig. 1 for location of the study area, and for the local stratigraphic sequence. Inset map shows the locations of the four circular domains in which we conducted a detailed analysis of fracture network properties. The latitude and longitude coordinates for the center of each analysis domain are as follows. D1: Lat. 38°47′59.45″N, Long. 109°,42′4.49″W; D2: Lat. 38°,48′0.84″N, Long. 109°,42′16.32″W; D3: Lat. 38°47′52.79″N, 109°42′9.37″W; D4: Lat. 38°47′35.71″N, Long. 109°42′5.01″W. (For interpretation of the references to colour in this figure legend, the reader is referred to the web version of this article.)

generally homoclinal, and dips 10–15° toward the southwest.

There are two Jurassic stratigraphic units that are important for studying the fracture networks in the region of Salt Valley anticline: the Moab Member of the Curtis Formation (assigned to the Entrada Sandstone prior to Doelling, 2000; Graham, 2004), and the Slickrock Member of the Entrada Sandstone. These two sandstone units comprise at least 65 km² of exposed, fractured rocks on both limbs of the fold, with the Moab Member accounting for nearly 75% of this area. The Moab Member of the Curtis Formation varies in thickness from 18 to 37 m throughout the region, and is a well-indurated, fine-to medium-grained, calcite-cemented, quartz arenite with rounded to subrounded grains, and meter to decameter scale, low-angle cross bedding (Doelling, 1985, 2000; Doelling et al., 1988; Graham, 2004). The Moab Member is the youngest, systematically fractured bedrock unit that crops out in the Salt Valley region, and overlies the Slickrock Member of the Entrada Sandstone. The Slickrock Member regionally varies in thickness from 61 to 107 m, and is comprised of well-indurated, orange-red to red-brown weathering, very fine-to fine-grained, calcite and iron-oxide cemented, quartz arenite. Massive, planar-bedded, and cross-bedded intervals are present, with cross bedding typically occurring on the scale of meters (Doelling, 1985, 2000; Doelling et al., 1988; Graham, 2004). These two units are readily distinguished in color aerial imagery (Fig. 2).

Fracture networks in the region surrounding Salt Valley anticline have been studied extensively for more than three decades (Dyer, 1983, 1988; Doelling et al., 1988; Cruikshank et al., 1991; Zhao and Johnson, 1992; Cruikshank and Aydin, 1995; Davatzes and Aydin, 2003; Lorenz and Cooper, 2009). Together these studies indicate that joints and deformation bands are the predominant fracture types, and that there is

significant evidence for the reactivation of joints. Overall, the fracture network is interpreted to have formed in a stress field that underwent a ~90° counter-clockwise rotation throughout the history of fracturing (Dyer, 1983; Zhao and Johnson, 1992; Cruikshank and Aydin, 1995). The spatial variability of fracture properties has intrigued and perplexed many researchers, most of whom only examined the variability of fracture orientations. Fractures of dramatically different orientation are found in adjacent portions of the Moab and Slick Rock Members (Cruikshank and Aydin, 1995), and within the better-exposed Moab Member, the fracture network is comprised of spatially distinct domains that commonly contain fractures of one or two dominant orientations (Dyer, 1983; Lorenz and Cooper, 2009). These domains may be five to ten or more square kilometers in area, and adjacent domains may have different numbers of systematic fracture sets, and/or dominant fracture trends that differ by as much as 45°. Transitions between domains can occur over horizontal distances as small as 100 m, making them strikingly abrupt when compared to the scale of Salt Valley anticline. Although previous workers have noted that stress orientations and deformation history must have been consistent within a given domain (e.g., Cruikshank and Aydin, 1995; Lorenz and Cooper, 2009), the mechanism(s) of fracture domain formation is(are) enigmatic. Most researchers posit a relationship to folding history and the 3-D halokinetic growth of the underlying salt wall, but such a relationship has yet to be tested with mechanical, kinematic or physical modeling. In this study we use geostatistical methods to quantify the spatial variability of fracture network properties across a fracture domain boundary, and attempt to correlate that spatial variability with larger structures that may have played a role in creating it.

3. Methods

We began our analysis of the fracture network by assembling in a Geographic Information System (GIS) database, georeferenced and rectified, 25 cm per pixel resolution aerial imagery that covered the entire study area (Fig. 2). The fracture network was digitized in ESRI's ArcGIS™ software while observing the images at a constant 1:3000 scale. At this observation scale it is difficult to consistently differentiate between parallel fractures that are separated by fewer than 5 m. This resolution limit was considered in our decision to use a 5 m spacing of analysis grid nodes at which we subsequently calculated fracture network attributes.

3.1. Fracture network attribute maps

For the analysis of fracture network attributes, we divided the Klondike Bluffs area into four, 600 m diameter, circular domains, labeled D1 through D4. Aerial photos and digitized traces of fractures for each domain are provided in Fig. 3. The placement and overlap of the domains was designed to capture small scale variations in fracture network properties that might be related to the faults that cut across the northern edge of the region, forming the bluffs, and locally truncating exposures of the Moab Member.

Although many fracture network attributes exist, we chose to analyze fracture length per unit area (i.e., areal fracture intensity) and fracture intersections per unit area (i.e., intersection density). We chose these attributes because of their relation to secondary porosity and permeability (Rohrbaugh et al., 2002), and because of their intrinsic reduction in the impact of interpreter bias. In studies of fracture length distributions, results derived from photogeological maps will be biased by where an interpreter places the end of a digitized fracture, among other things. Interpretation differences will affect individual fracture lengths, and there may be a substantial percentage error, especially in the length of shorter fractures. The same biases are present in
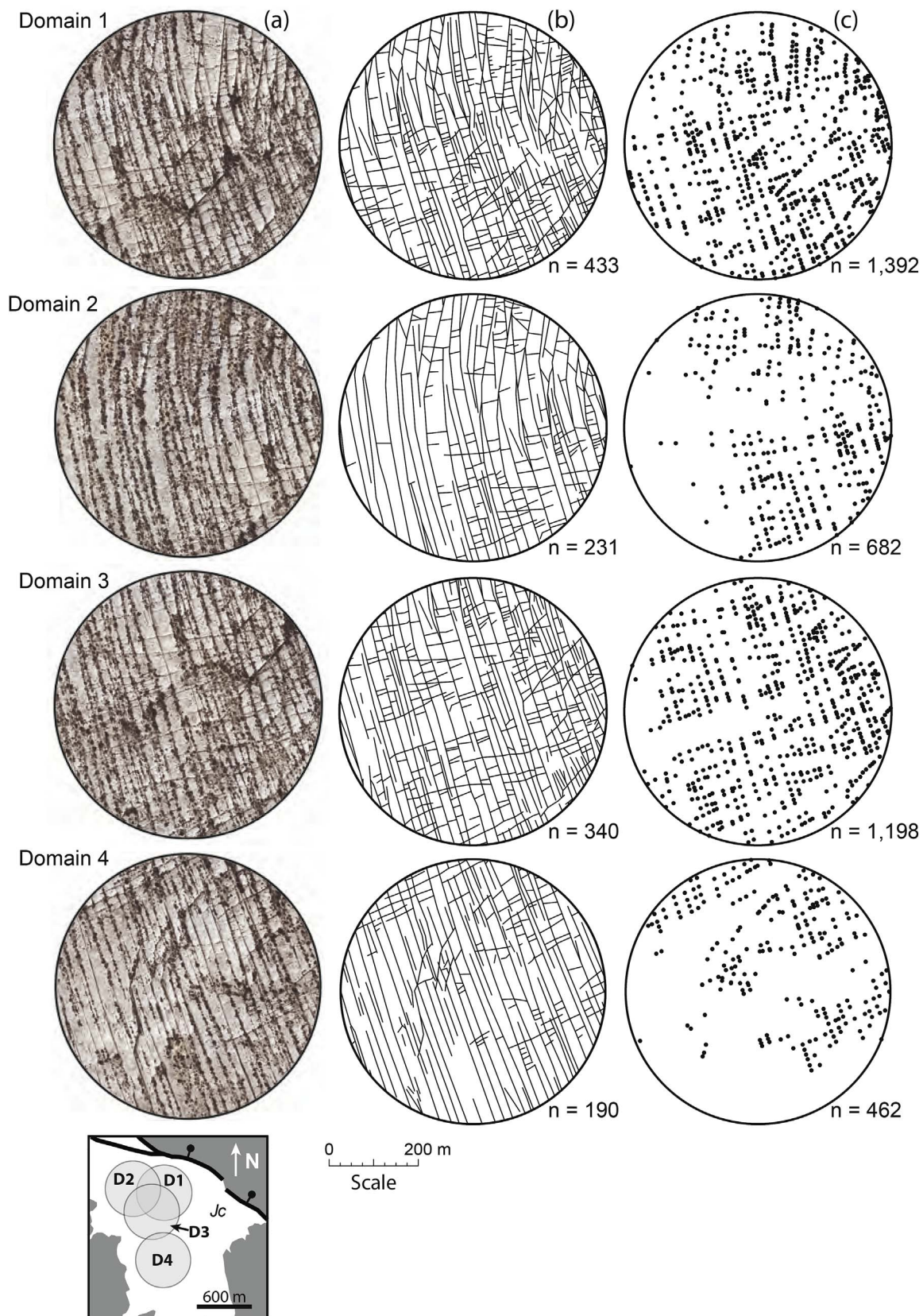
Fig. 3. Detailed geometry of the fracture network in the four zones (D1-D4) in which we analyzed fracture network attributes. The three columns of images are labeled a, b, and c, from left to right. (a) Aerial images of the fracture network in each zone. (b) Digitized fracture traces in each zone. (c) Fracture intersections extracted from the digitized fracture traces shown in (b). Scale applies to all circular maps. Inset map shows the location of each analysis zone in the study area. The value *n* is the number of fractures or intersections for each respective domain, including its buffer zone (not pictured). See Fig. 2 for an aerial image of the entire study area, and Fig. 1 for the regional geological context.
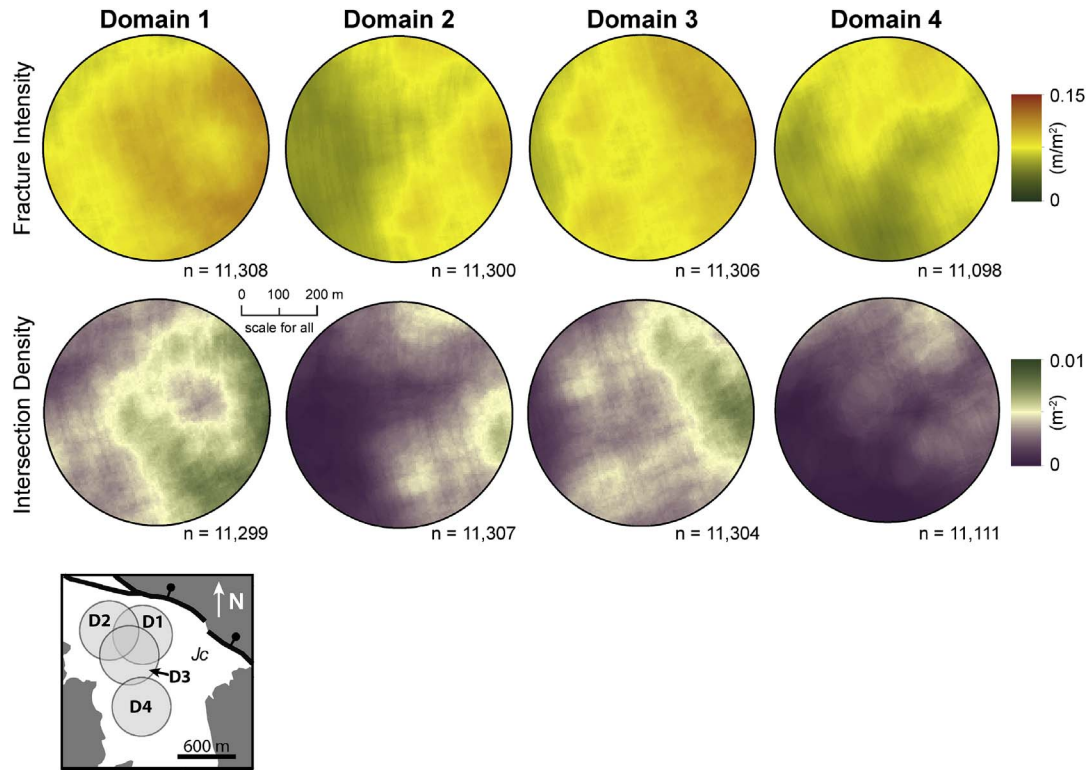
Fig. 4. Fracture intensity and intersection density maps for four analyzed domains shown in the inset map. The value n is the number of pixels for each raster, where each pixel represents a 5 × 5 meter area. See Fig. 2 for an aerial image of the entire study area, and Fig. 1 for the regional geological context.

calculations of fracture intensity, but the magnitude of the bias is less impactful because it should constitute a constant and much smaller percentage of the total fracture length in a given analysis region. We minimized bias in our intersection density calculations by using the ArcGIS™ intersect tool to automatically extract the locations of intersecting, digitized fractures; we did not digitize these locations ourselves.

The fracture attribute raster maps were created from all digitized fractures within a given analysis domain, regardless of orientation (Fig. 4). Each fracture intensity map contains equally spaced 5 × 5 m grid cells, where the value of each cell is the cumulative fracture length that falls within the 100 m radius of a circular analysis window that is centered on the cell. Each intersection density map contains a similar set of equally spaced 5 × 5 m grid cells, but the value of each cell is the cumulative number of intersections that fall within the 100 m radius of the analysis window. We chose our analysis window size after trying several radii between 10 and 100 m, values that were near the average fracture spacing in the study area. Circular artifacts were common in raster maps created with analysis windows substantially smaller than 100 m. The 100 m analysis window produced maps without artifacts and empirical semivariograms with less noise. Boundary effects occur when the center of an analysis window falls within 100 m of the edge of the map. When this happens, calculated values are underestimated because some portion of the analysis window extends into an unmapped region. We eliminated these effects by including a 100 m wide buffer zone along the margin of each map; digitized fracture traces and intersections that fall outside of a mapped domain, but within this zone, were included in the calculations.

3.2. Quantifying spatial variability and correlation

The semivariogram is a geostatistical tool for quantitatively

characterizing the spatial correlation of measurable attributes distributed over an area or volume (Deustch and Journel, 1998; Kitanidis, 1997; Şen, 2009; O'Sullivan and Unwin, 2010). Although the semivariogram has been applied to fracture network analysis for at least thirty years (e.g., La Pointe and Hudson, 1985; Long and Billaux, 1987; Billaux et al., 1989; Kupfersberger and Deutsch, 1999; Dewit et al., 2012; Pollyea and Fairley, 2012; Pollyea et al., 2013; Koike et al., 2015), and is an integral component of stochastic modeling and spatial interpolation routines (e.g., Deutsch and Journel, 1998; Deutsch, 2002; Stein, 2012), it is not widely understood or employed by field structural geologists. As a result, it has not been routinely applied in the analysis of regional scale (i.e., 100s–1000s of meters) fracture networks. To facilitate such work, we briefly review some general aspects of the semivariogram, and then explain the specific semivariogram analysis techniques employed in this paper.

To appreciate the utility and limitations of semivariogram analysis, it is useful to understand the raw data from which the semivariogram model is constructed. As shown by the schematic, 2-D example in Fig. 5, these data are created by successively choosing each (x_i, y_i) point in the data set as a control point, and calculating:

$$\gamma = \frac{1}{2}(z_i - z_j)^2, \tag{1}$$

where z_i is the attribute value at the control point, and z_j is the attribute value at another data point. Anisotropy in the data can be investigated by performing this calculation in a swath of data distributed in a particular direction (θ), where the swath is defined by an azimuthal bandwidth (b), and an azimuthal tolerance (φ; Fig. 6).

In stochastic modeling and prediction it is impractical to work with the raw semivariogram data comprising every possible point pair at every possible separation distance. As a result, a more useful, experimental semivariogram is computed by averaging the raw
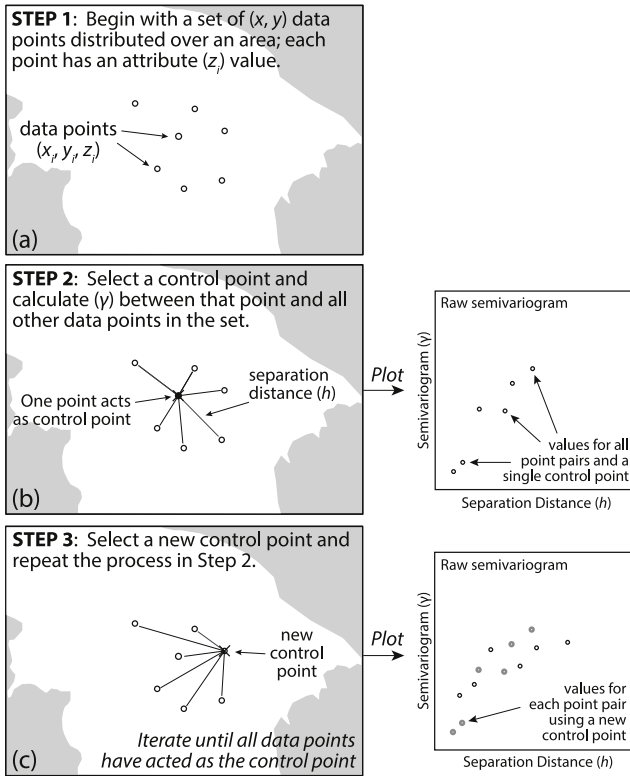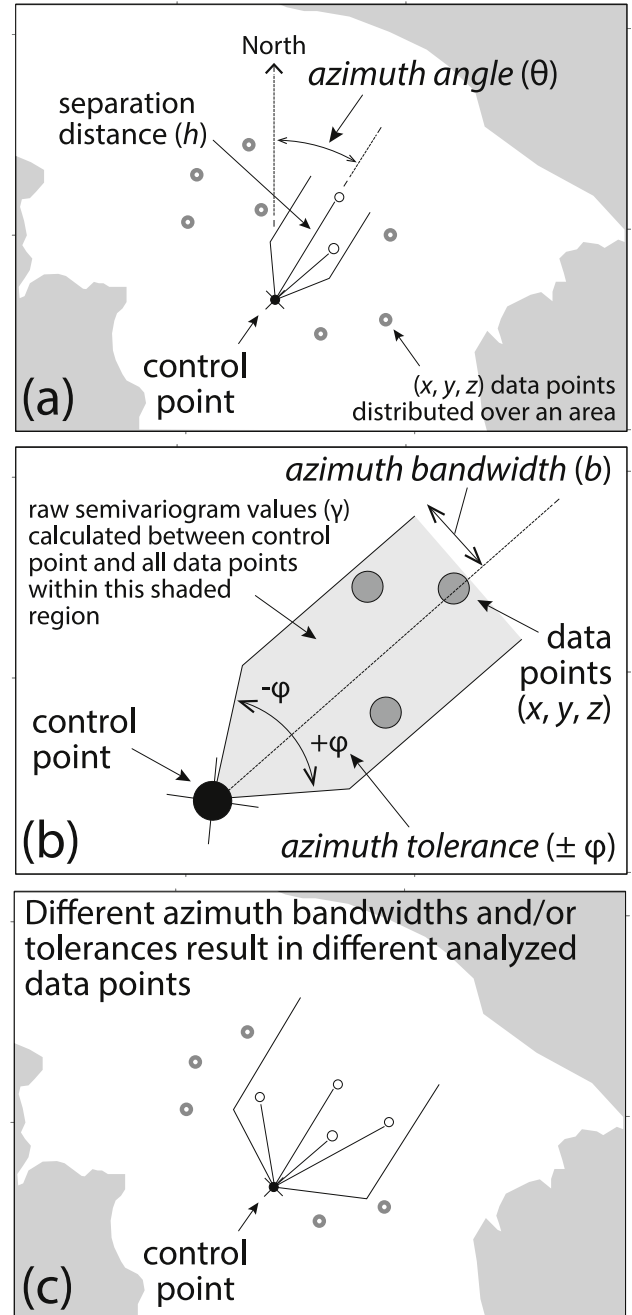
Fig. 5. Schematic illustration of the steps involved in the creation of a semivariogram. (a) Data distributed over a 2-D plane are defined by (x, y) coordinates and some attribute value (z). (b) Equation (1) is used to characterize the difference in (z) between all pairs of data associated with a chosen control point. Semivariogram values (γ) for each data pair are plotted versus the separation distance (h) between each pair of data points. (c) A new control point is chosen and semivariogram values are calculated and plotted for all the new data pairs.

semivariogram data at uniformly distributed, spatial lag distances (Fig. 7a and b). The averaged data are drawn from a zone (i.e., a lag) whose width is defined by a lag tolerance (Fig. 7b). For a continuous variable, the experimental semivariogram (γ) as a function of lag distance (h) is defined by Deutsch and Journel (1998) as:

$$\gamma(h) = \frac{1}{2 \cdot N(h)} \sum_{i=1}^{N(h)} (z_i - z_{i+h})^2, \tag{2}$$

where, z_i is a datum at location i, z_{i+h} is a datum within the lag centered on a distance (h) from position i, and $N(h)$ is the number of data pairs within that given lag (Fig. 7c). The experimental semivariogram measures the average dissimilarity between all data pairs separated by a given lag distance. As a result, semivariogram values generally increase with increasing lag distance, which indicates that data values become less similar as the distance between them increases (Fig. 7d).

The spatial correlation structure of a data set is described by the distribution of semivariogram values at short lag distances and the manner in which semivariogram values increase with distance. This structure is traditionally formalized by modeling (i.e., fitting) the experimental semivariogram with linear combinations of positive-definite, *a priori* permissible functions, depending on the application (e.g., exponential, Gaussian, spherical, and hole effect; Goovaerts, 1997; Deutsch and Journel, 1998). As a result, spatial structure quantified by the semivariogram is fully characterized by: (1) the nugget effect, which is a discontinuity at the origin and represents spatial variability

Fig. 6. Schematic illustration of the process and variables involved in the creation of a directional semivariogram. (a) Semivariogram values (γ) are calculated between pairs of points along an azimuthal direction through a 2-D map. (b) The swath of data for which the calculation is done is defined by an azimuth tolerance and azimuth bandwidth. (c) Increased azimuth bandwidth and/or tolerance changes the data points involved in the calculation.

at lower resolution than the sample spacing; (2) the sill, which is the variance of the dataset about which the semivariogram oscillates at long lag distances, and represents the absence of spatial correlation (i.e., spatial randomness); and (3) the range, which is the distance within which spatial correlation is inferred (Fig. 7e). When a model semivariogram incorporates multiple functions, the contribution of each function is parameterized with an individual range and sill such that the nugget effect and sill contributions sum to the variance of the
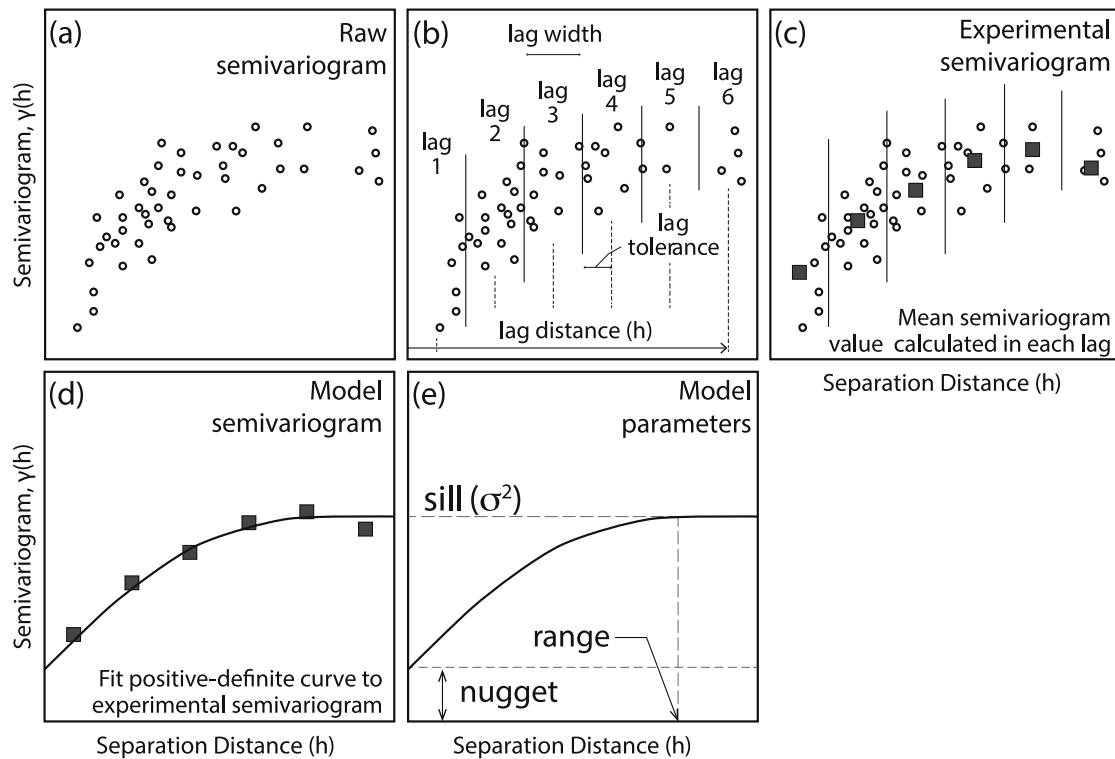
Fig. 7. Schematic illustration of the steps involved in the semivariogram modeling. (a) Raw semivariogram data (Eq. (1)) are plotted as a function of the separation distance between each pair of sample points. (b) The range of separation distances is divided into lag bins defined by a lag distance (h) at the center point and a lag tolerance (half-width of bin). (c) the empirical semivariogram (Eq. (2)) is calculated for each lag bin, which are plotted as a function of h. (d) A continuous function (model semivariogram) is fit to empirical semivariogram data. (e) Important characteristics of the model function are related to the spatial structure of the data: the nugget effect is the discontinuity at the origin, which suggests spatial variability a length scales smaller than the grid resolution; the range is the maximum length scale of spatial correlation; and the sill is sample variance (σ^2) for a bounded semivariogram. Note that the raw data shown in these figures are highly schematic, and are not intended to represent results from this or any real study.

dataset (Goovaerts, 1997).

To visualize the 2-D structure of the spatial correlation of data values, 3-D surfaces or 2-D maps can be constructed from multiple, directional semivariograms calculated in a variety of orientations to identify anisotropy in the spatial correlation structure (Fig. 8). The spatial variability defined in this fashion is bilaterally symmetric because the semivariogram calculated in opposite directions is equal (i.e., a semivariogram calculated at an azimuth of 5° would be the same as one calculated at an azimuth of 185°). For the present study, we calculated directional semivariograms in our fracture intensity and intersection density maps (Fig. 4) using the Geostatistical Software Library™ (GSLIB; Deutsch and Journel, 1998). Input parameters for the calculation are provided in Table 1 (Deutsch and Journel, 1998). To facilitate comparison between the semivariograms for each of the four examined domains (Figs. 3 and 4), all semivariograms are normalized over their respective variances so that the nugget effect and the sill contributions of each model sum to 1. For each fracture intensity and intersection density map, we conducted the calculation along azimuths from 0° – 175°, every 5°, for a total of 36 semivariograms. Previous investigators have suggested that a minimum of 150–225 sampled data pairs is necessary to adequately characterize isotropic correlation structure, and that substantially more may be required in the presence of anisotropy (Journel and Huijbregts, 1978; Webster and Oliver, 1992). Of the 5760 lags in which we calculated $\gamma(h)$, 99.8% of them meet or exceed this criterion by up to three orders of magnitude (Fig. 9). We used a fifth order polynomial equation to model each semivariogram, and each of these models fit the data with a regression coefficient (R^2) of at least 0.9; for the vast majority of the fits, R^2 exceeds 0.98 (Hanke, 2015).

Why did we choose a non-traditional polynomial function to model our experimental semivariograms, rather than a traditional exponential, Gaussian, or spherical function? This decision and its implications are rooted in the concept known as stationarity (e.g., Matheron, 1973; Myers, 1989; see Appendix A for more details on stationarity). Traditional functions (e.g., spherical, exponential, Gaussian) are often chosen for semivariogram models because the behavior of these functions is known to be *a priori* permissible at the origin and infinity, and in three Cartesian directions (Goovaerts, 1997, p. 88–89). As a result, the traditional semivariogram functions are well suited for predicting the RV, and they are commonly incorporated as parameterized functions within geostatistical software packages (e.g., GSLIB; Deutsch and Journel, 1998). However, because we employ the semivariogram only to *describe* spatial correlation, not to *predict* the value of a RV at a given location, our approach does not require the typical *a priori* decision to restrict ourselves to choices of stationary semivariogram models. We used a polynomial semivariogram model in this study because it provided the best possible fit to the vast majority of directional semivariograms we analyzed (Hanke, 2015). The function we use is positive-definite at all spatial lags and, according to criteria defined by Journel (1996), is acceptable for modeling semivariogram spatial correlation structure. Other workers have also adopted non-stationary semivariogram models, which are increasingly being used for RV-prediction (e.g., Han et al., 2014; Hu et al., 2014; Zamanian et al., 2014).

3.2.1. Quantifying the amount of spatial variability: variability volumes

Data are often qualitatively described as exhibiting a high or low
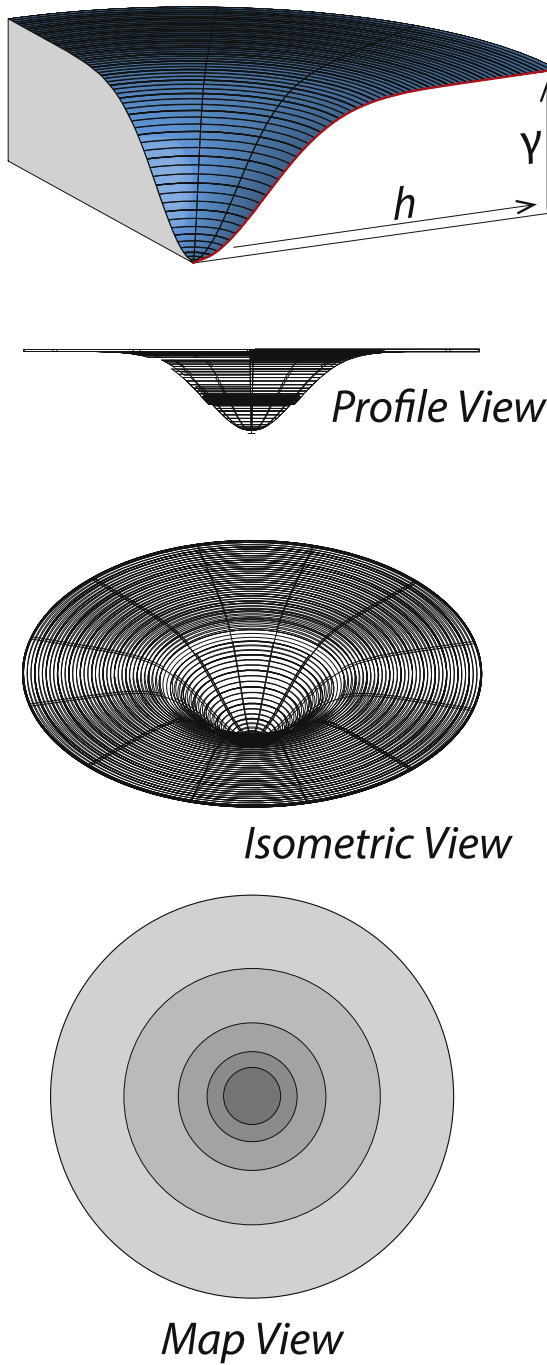
Fig. 8. Examples of how multiple directional semivariogram models can be used to visualize the spatial structure of a set of attributes (z) that are distributed over a 2-D region.

Table 1
Summary of parameters used in the calculation of experimental, directional semivariograms. See Figs. 6 and 7 for an illustration of each parameter.

Parameter	Quantity
Number of lags per semivariogram	20
Center-to-center distance between lags	30 m
Lag tolerance	15 m
Azimuth bandwidth (b)	20 m
Azimuth tolerance (φ)	10°

degree, or *amount* of spatial variability. To quantify these assertions and to provide a basis for rigorously comparing the degree to which a fracture network attribute (e.g., fracture intensity) varies throughout a 2-D region, we use the area under a semivariogram model to generate a quantity we call a variability volume. Consider the two imaginary topographic profiles and their associated schematic semivariograms shown in Fig. 10. The variability of elevation for both profiles can be modeled by semivariograms with constant semivariance for all lags (i.e., a pure nugget effect; Goovaerts, 1997). The spatial variability of elevation for Profile *B* is intuitively greater than that of Profile *A*, and the area under each semivariogram provides a means by which we can quantify this difference. In 2-D maps, where we have model semivariograms in multiple directions (θ) from 0° - 175°, we can extend this approach by comparing what we hereafter call a variability volume (V):

$$V = \sum_{i=1}^{n} V_i. \tag{3}$$

This volume is the sum of several subvolumes (V_i), each of which is created by rotating a semivariogram model ($\gamma(h)$) through an azimuthal bin extending from direction θ_1 to θ_2 (Fig. 11), and then integrating

$$V_i = \int_{\theta_1}^{\theta_2} \int_{h}^{h_{\max}} \gamma(h)\, dh\, d\theta, \tag{4}$$

where $h_{\max}$ is the largest lag distance in the experimental semivariogram and $\theta 1$ and $\theta 2$ are defined in degrees. Variability volumes computed at different locations can be meaningfully compared only when all the comprising, directional, model semivariograms were calculated with the same parameters (Table 1). Normalized variability subvolumes can be created by dividing equation (4) by the area over which the volume is calculated, or

$$\pi \frac{((\theta_2 - \theta_1))}{360°} h_{\max}^2, \tag{5}$$

where $\theta 1$ and $\theta 2$ are azimuthal directions defined in degrees.

Working with such normalized volumes enables workers to compare results collected from areas of different size, or to examine the impact of varying lag sizes on their results; investigations that are beyond the scope of this work. Such analyses should be done with extreme caution and practitioners should be fully aware of pitfalls that arise when comparing variability volumes that are derived from different analysis parameters (e.g., lag size, azimuthal tolerance, analysis window size, pixel size in each raster map, $h_{\max}$). Here, the size of our four analysis domains is identical, as is every analysis parameter we employed to calculate our variability volumes. Normalization was consequently unnecessary.

3.2.2. Quantifying structure in spatial variability: relative variability ratios

We propose to quantify the structure exhibited by a 2-D, spatially distributed data set through a quantity we call the relative variability ratio ($R_{A,B}$). This value compares the amount of spatial variability in two different azimuthal directions (θ_A, θ_B; Fig. 6a), and is given by

$$R_{A,B} = \frac{\int_{h}^{h_{\max}} \gamma_A(h)\, dh}{\int_{h}^{h_{\max}} \gamma_B(h)\, dh}, \tag{6}$$

where $\gamma_A(h)$ and $\gamma_B(h)$ are the model semivariograms along those directions. When $R_{A,B} = 1$ there is no difference in the amount of spatial variability between the two compared directions. As $R_{A,B}$ increases or decreases from one, there is an increasing amount of spatial variability in one of the two investigated directions. Unlike methods presented by Kupfersberger and Deutsch (1999), this approach can quantify
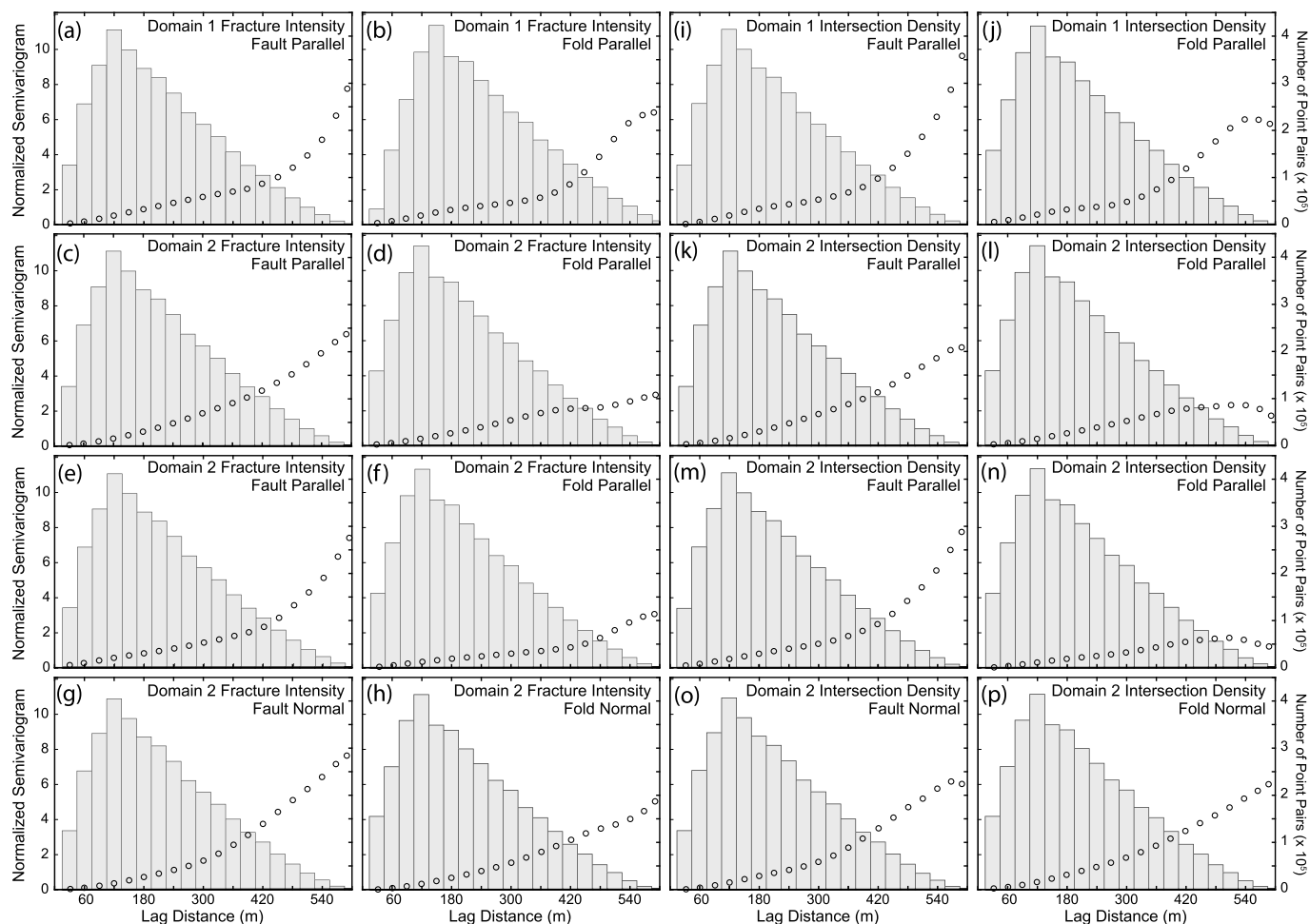
Fig. 9. Dual *z*-axis graphs of normalized empirical semivariograms of fracture intensity (a–h) and intersection density (i–p) in directions related to local faults and Salt Valley Anticline. Superimposed histograms display the number of point pairs for each lag of the semivariograms. Note that the vertical histogram scale is multiplied by 10^5.
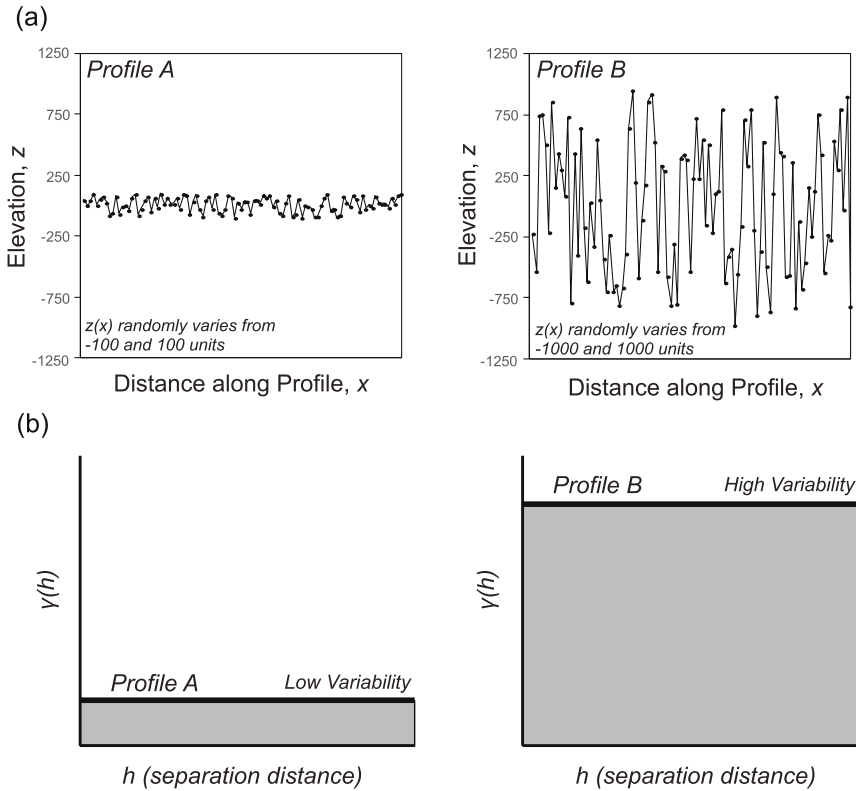
directional differences in spatial variability for cases when the two compared directions differ by angles other than 90°. This can help to identify subtle, directional variations in the spatial structure of a 2-D, spatially distributed data set. When attempting to identify such variations, it is important to recognize that the choice of h_{max} has a significant impact on the results of Equation (6). One should carefully consider the quality and reliability of points comprising the most distal portions of an experimental semivariogram before deciding on this value.

4. Results

To enable a cursory comparison of our fracture intensity and intersection density maps (Fig. 4), and to search for spatial variability at scales larger than the maps, we first calculated a suite of standard statistics in each mapped domain (Table 2). One aim of these comparisons is to characterize the extent to which the fracture network may have been affected by faulting along the northern edge of the study area (Fig. 2). Do the examined fracture network properties vary in a manner that correlates with these faults, with nothing, or with some other, larger-scale structure, such as the Salt Valley anticline? Examination of the data in Table 2 reveals that the domain closest to the fault (D1) exhibits consistently higher mean, minimum, and maximum fracture

intensity values when compared to the domain furthest from the fault (D4). This same decreasing trend is visible in the intersection density values, as well as the variances of fracture intensity and intersection density. Although more detailed analyses in other regions or with smaller, or differently located analysis domains could provide better constraints, these spatial trends in measures of sample variability suggest that intersection density and fracture intensity may exhibit heteroskedasticity (Rubin, 2003). If present, this property could have important implications for the biases and errors associated with predictive models of spatially varying fracture network properties.

Aside from a faint linear pattern that seems to parallel the trends of major fractures in some domains, and a general tendency to increase from the WSW to ENE across some domains, there is little visible structure within any of the fracture intensity or intersection density maps (Fig. 4). To quantify and visualize spatial variability as a function of orientation in a 2-D horizontal plane, we took the 36 normalized, experimental semivariograms we created from each of these maps, and arranged the 1584 associated γ(h) values into a 3-D point cloud. We interpolated between these experimental semivariogram values and created a new set of data that were arranged in a 2 m grid that covered each circular, mapped domain. Contouring these new data enabled us to create normalized semivariogram maps that quantify the 2-D spatial variability of fracture intensity and intersection density in each of the

(a)

Profile A

z(x) randomly varies from -100 and 100 units

Profile B

z(x) randomly varies from -1000 and 1000 units

(b)

Profile B — High Variability

Profile A — Low Variability

Fig. 10. Schematic illustration of the relationship between the area under a directional semivariogram model equation and the amount of spatial variability in the analyzed direction. (a) Example 2-D elevation (z) profiles comprising 100 random data points that are evenly distributed along the x-axis, and that vary between different prescribed high and low elevations. (b) Nugget semivariogram models adequately characterize each profile, but have different areas beneath them. The model with the greater area under the semivariogram model curve exhibits greater spatial variability in elevation.
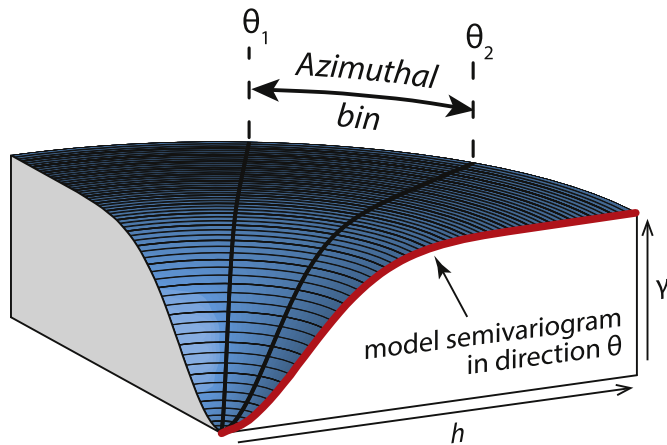
Fig. 11. Parameters involved in the calculation of a variability volume. A model, directional semivariogram is rotated through an azimuthal angle from θ_1 to θ_2. As defined in Equation (4), an integrated volume is calculated from a series of azimuthal bins from 0° to 180°. For ease of illustration, this example assumes an identical directional, semivariogram model along every azimuth through the analyzed region.

four domains we investigated (Fig. 12).

The normalized semivariogram maps of fracture intensity and intersection density show that the spatial correlation of these two fracture network properties is highly anisotropic in each of the four domains we examined. Although the geometry of the anisotropy is similar for each property in a given domain, each domain displays a unique structure to that anisotropy. In domain 1, spatial correlation is minimum along an azimuth near 015° and maximum along an azimuth near 110°,

directions that are respectively subperpendicular and subparallel to the nearby fault (Fig. 12). This same anisotropy structure exists in the other three domains, but the orientation is progressively rotated counter-clockwise from domain 2 to 3 and 4. In domain 4, the direction of minimum correlation is subparallel to the local trend of Salt Valley anticline (125°), whereas the direction of maximum correlation is subperpendicular to the nearby fault (Fig. 12). Only in domain 3 does the anisotropy structure correlate to the dominant orientation of fractures. The variability anisotropy is slightly (domain 2) to strongly (domains 1 and 4) misoriented relative to the dominant fracture orientations in each of the other domains (compare Figs. 3 and 12).

To quantify the degree to which the anisotropy in any domain correlates with the trend of either Salt Valley anticline (105°) or the local faults along the northern edge of the map area (125°), we calculated in each map, the relative anisotropy ratio (Eq. (6)) in directions related to these two structures. In domains 1, 2, and 3, where the maximum variability is oriented subparallel to the trends of the fold and fault (Fig. 13), we calculated variability ratios in these two directions. In domain 4, where the maximum variability is subperpendicular to the structures, we calculated variability ratios in directions that were 90° clockwise from those in the other domains. As shown in Fig. 13, our calculations show that in every domain, a greater amount of variability occurs in directions related to the fault. In domain 1 the amount of variability related to the fault is only 2–5% higher than that related to the fold. In domain 2 there is roughly 60% more variability parallel to the fault than parallel to the fold, whereas in domain 3 there is between 80 and 120% more variability. In the domain 4, which is furthest from the fault, the amount of variability related to the fault is also greater than that related to the fold, but the relative increase in variability is only 4–35%. The connections between the amount of spatial variability

Table 2

Summary statistics for fracture intensity and intersection density attributes within each of the circular domains shown in Fig. 4. The table includes parameters of: number of cells within a sample population (n), sample arithmetic mean ($\bar{x}$), sample standard deviation (s), sample variance (s^2), coefficient of variation (C_v), minimum attribute value (Min) and maximum attribute value (Max). These statistics do not contain any spatial information other than they include sample populations from domains at different locations.

|		Domain 1	Domain 2	Domain 3	Domain 4
Fracture Intensity	n	11,308	11,300	11,306	11,098
	$\bar{x}$ (m/m^2)	8.908×10^{-2}	6.763×10^{-2}	8.281×10^{-2}	6.578×10^{-2}
	s (m/m^2)	1.195×10^{-2}	1.353×10^{-2}	1.088×10^{-2}	1.094×10^{-2}
	s^2 (m/m^2)^2	1.429×10^{-4}	1.830×10^{-4}	1.183×10^{-4}	1.197×10^{-4}
	C_v[a]	0.1342	0.2000	0.1313	0.1663
	Min (m/m^2)	6.308×10^{-2}	4.133×10^{-2}	5.670×10^{-2}	3.983×10^{-2}
	Max (m/m^2)	1.174×10^{-1}	1.015×10^{-1}	1.106×10^{-1}	9.183×10^{-2}
Intersection Density	n	11,299	11,304	11,307	11,111
	$\bar{x}$ (m^{-2})	4.944×10^{-3}	2.431×10^{-3}	4.122×10^{-3}	1.689×10^{-3}
	s (m^{-2})	1.470×10^{-3}	1.514×10^{-3}	1.398×10^{-3}	1.115×10^{-3}
	s^2 (m^{-2})^2	2.161×10^{-6}	2.293×10^{-6}	1.956×10^{-6}	1.243×10^{-6}
	C_v[a]	0.2973	0.6229	0.3393	0.6601
	Min (m^{-2})	1.368×10^{-3}	6.366×10^{-5}	7.003×10^{-4}	0
	Max (m^{-2})	8.912×10^{-3}	6.430×10^{-3}	8.053×10^{-3}	4.870×10^{-3}

[a] Unitless quantity.
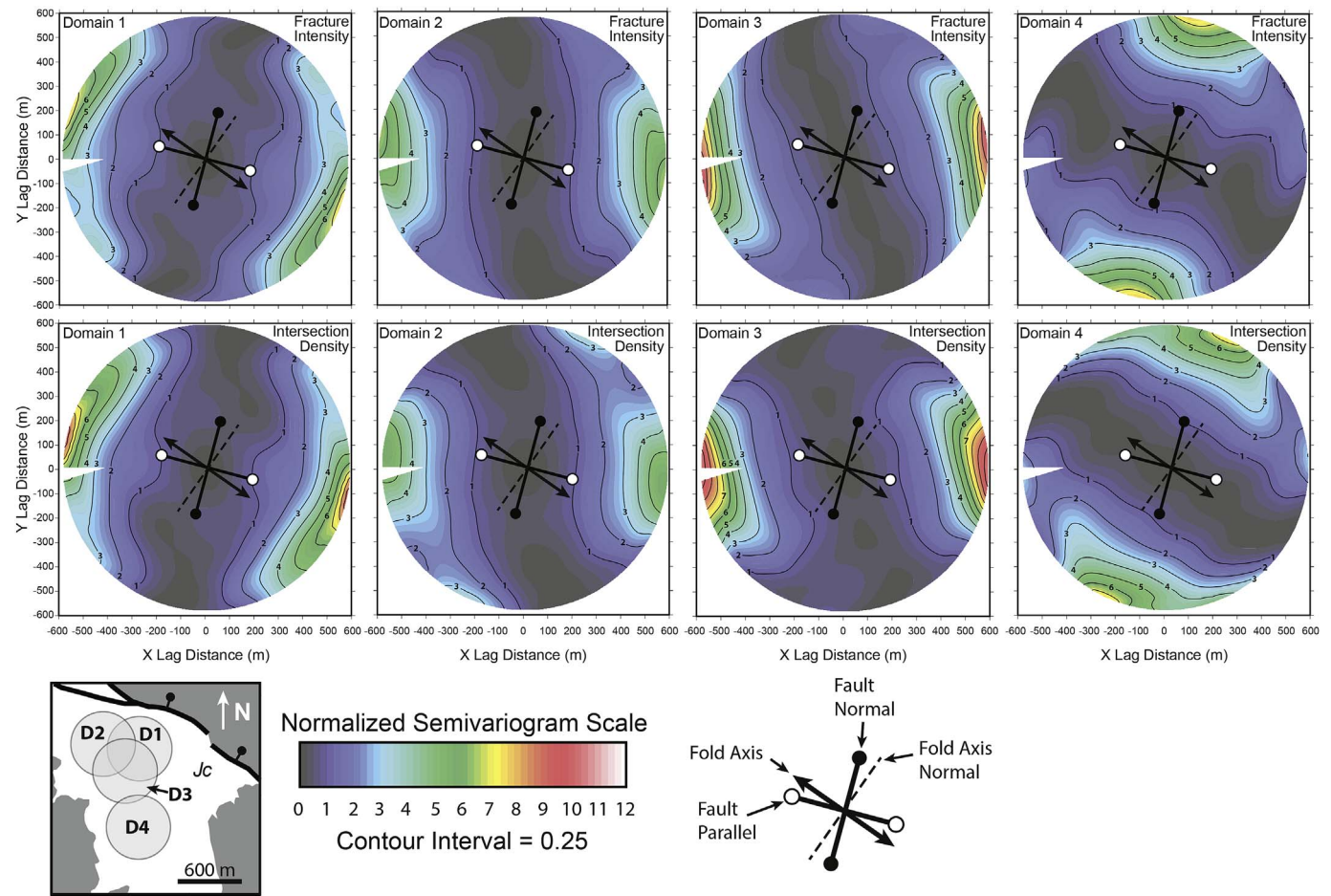
Fig. 12. Normalized semivariogram maps showing the 2-D spatial variability of fracture intensity and intersection density in each of the four domains shown in the inset map. Each map is oriented with north toward the top of the page. Darker shades correspond to lower amounts of spatial variability. Locally and regionally important structural trends are indicated on each map for comparison.
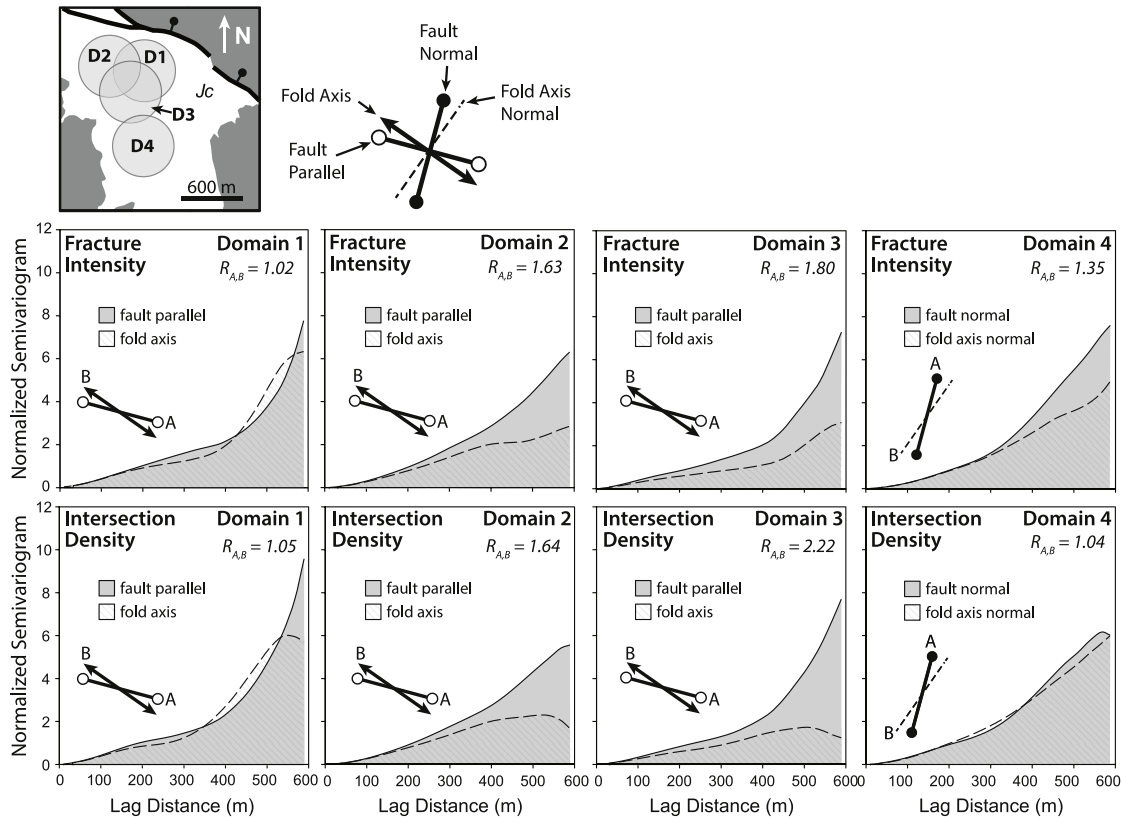
Fig. 13. Graphs comparing the normalized semivariograms of fracture intensity and intersection density in directions related to local faults and Salt Valley anticline. Shading indicates the two compared directions in each graph, and the lines labeled A and B are drawn parallel to these directions, assuming north is toward the top of the page, as in the inset map. This map also shows the location of the domains in which the semivariograms were calculated.

of fracture network properties and local folding and faulting are further illustrated in Fig. 14, which graphs the area under every directional semivariogram model in domains 1 and 4.

To quantify and compare the total amount of spatial variability exhibited by each fracture network parameter across the map area (Fig. 2), we calculated eight variability volumes, one for each parameter in each of our mapped domains. The volumes were created from non-normalized semivariogram models, and are compared in the pair of matrices presented in Fig. 15. These comparisons indicate that, as distance from the northern faults increases, there is a corresponding decrease in the amount of spatial variability in both the fracture intensity and intersection density parameters. For fracture intensity, the amount of spatial variability decreases an average of 40% over the 1 km distance from domains close to the fault (i.e., domains 1 and 2) to the domain that is furthest from the fault (i.e., domain 4). The amount of spatial variability in intersection density decreases by an average of 75% over this same distance (Fig. 15).

5. Discussion

The hydrologically and mechanically important properties of natural fracture networks can vary substantially throughout a volume of rock, and in ways that are not readily discernible in fracture network maps. This variability can impact the design and execution of myriad activities in the geotechnical, mining, hydrocarbon, groundwater, CO_2 sequestration, and waste disposal fields. The directional semivariogram provides a means to identify, describe, and quantify the amount and

correlation structure of the spatial variability exhibited by a fracture network, but is seldom used by the field structural geologists who are often charged with collecting and analyzing natural fracture network data. Wider application of this important tool has the potential to create a deeper understanding of the processes that control the spatial variability of fracture networks, unlocking new lines of research and facilitating more accurate stochastic modeling.

Natural fracture networks form through the interaction of many different processes, in stress fields that vary in both time and space. Rock properties also change during burial, diagenesis, and uplift, and as each new fracture forms (e.g., Laubach et al., 2014). Although geomechanical modeling has dramatically improved over the last decade (e.g., Maerten et al., 2002; Maerten and Maerten, 2006; Eckert et al., 2014; Liu et al., 2016), these many spatio-temporal interactions and variations make it practically impossible to deterministically simulate the formation and evolution of fracture networks, particularly at kilometer and larger scales. An alternative approach is to build predictive, stochastic models that accurately and reliably reproduce the characteristics of natural fracture networks. To do this, the models must be conditioned and calibrated using real world data. To date, most of those data constrain things like the distribution of individual fracture properties such as orientation, length and aperture; there are few data constraining the spatial distribution of these properties, or the properties of fracture networks such as intersection density or fracture intensity.

Our analysis constrains the spatial variability of fracture network properties and can be used to condition the output of stochastic models.
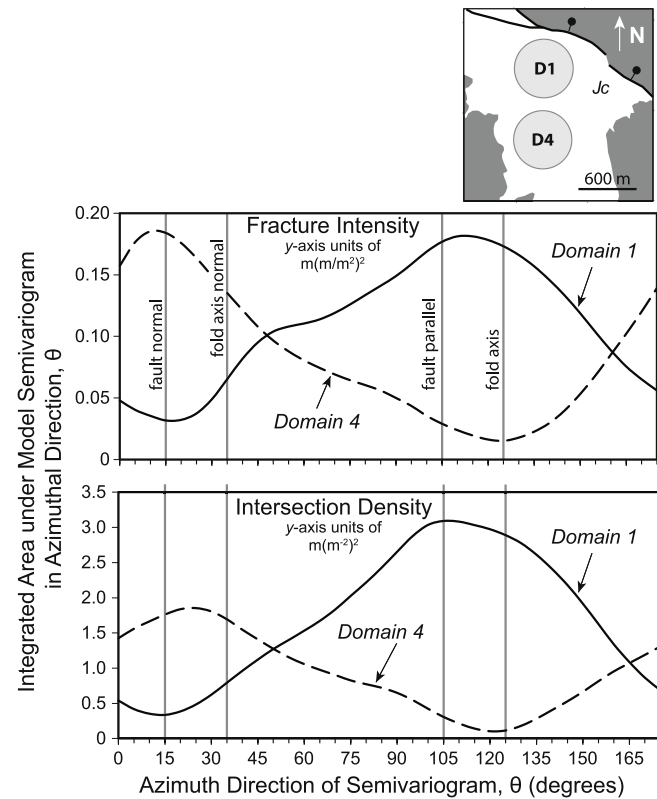
Fig. 14. Variation in the area under a directional semivariogram as a function of azimuthal direction across analysis domains close to (domain 1), and distal (domain 4) from the fault along the northern edge of the map area. Note that *y*-axis units are different for each graph. The inset map shows the location of each domain in the larger map area.

The correlation structure of spatial variability in the Klondike Bluffs fracture network correlates to the trends of the Salt Valley anticline and a nearby fault (Figs. 12 and 14). As shown in Fig. 16, the amount of spatial variability is higher near the fault and diminishes with distance away from the fault. These patterns suggest that structure in spatial variability may reflect scale-dependent perturbations in the processes or properties that influence fracture network development. These

perturbations may locally increase variability or reorganize its structure on scales that are proportional to their size. In this particular study, which examines a fracture network in a single rock unit in a 2.5 km^2 area, it is improbable that the changes in spatial variability we document are related to variations in rock properties, fluid pressure, burial or uplift history. As the largest, obvious, perturbing factor in this area is the anticline (10's of km in size), the spatial variability of fracture networks associated with it may be shown in domain 4, which is relatively far from any mapped faults. Overprinted on this background spatial variability is the influence of the fault (1's of km in size), which locally enhances variability and creates correlation structure in that variability that is also correlated to the fault. This correlation structure includes the fact that fracture intensity varies more dramatically along the fault than normal to it, a characteristic that is underappreciated in damage zone studies conducted using scan line methods (e.g., Berg and Skar, 2005; Riley et al., 2010; Savage and Brodsky, 2011; Choi et al., 2016). If they do not reproduce similar, realistic spatial variability patterns, stochastic models of fracture networks in folds and near faults should be re-evaluated, and discarded in favor of models that do. The ability of a model to capture these patterns can be determined by conducting directional semivariogram analyses through the model output.

As with any study of heterogeneity or homogeneity, scale is important in directional semivariogram analysis. Analyses must be conducted in areas that produce the minimum of ~200 data pairs per lag. The size of an analysis area must be smaller than the size of the perturbation causing the spatial variability one is investigating. Our 600 m diameter analysis domains enabled us to capture spatial variability at scales larger than 1–2 km, but most likely homogenized variability at scales smaller than 500 m. Before beginning a directional semivariogram analysis, researchers and modelers should carefully consider the scale of features or processes that may have affected the development of the fracture network they are investigating. Although doing so was beyond the scope of this work, analyses should most likely be done multiple times, using a different sized analysis domain each time. Such studies could reveal fascinating insights into the scale-dependence or independence of spatial variability in fracture network properties.

6. Conclusions

The structure of spatial variability of fracture network properties like fracture intensity and intersection density cannot be readily
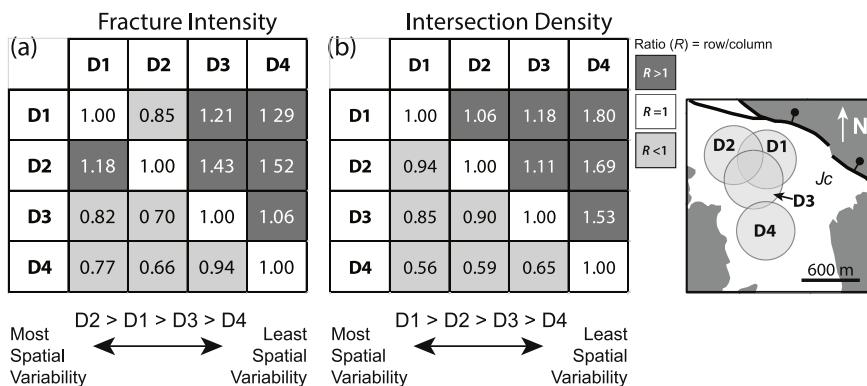

Fig. 15. Graphical comparison of the amount of spatial variability in each of the four analysis domains. Numbers in each matrix are the ratios of variability volumes calculated for each domain. Ratios greater than one indicate a greater amount of variability in the domain labeling the row, whereas ratios less than one indicate greater variability in the domain labeling the column. Domain locations are provided in the inset map.
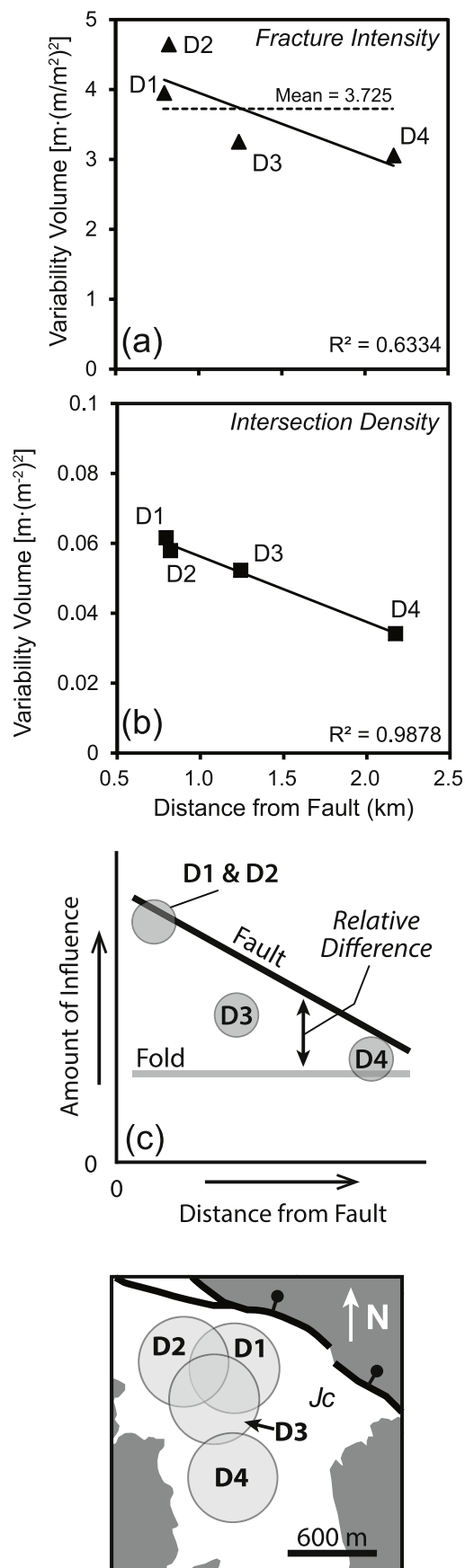
Fig. 16. Graphs illustrating the relative influence of Salt Valley anticline and a local fault on the amount of spatial variability in fracture intensity and intersection density in the Klondike Bluffs area. (a) Calculated variability volumes of fracture intensity for each analysis domain as a function of distance from the fault on the northern boundary of the study area. (b) Calculated variability volumes of intersection density for each analysis domain as a function of distance from the fault on the northern boundary of the study area. (c) Schematic representation of the spatially varying relative influence on fracture network properties of the fault and Salt Valley anticline. Inset map shows the locations of the analysis domains in relation to local faulting.

discerned from map patterns of fracture networks; it should be quantified with the directional semivariogram. Although accurate semivariogram calculation requires data sets with at least 200 data pairs per lag, there are many fracture network maps that should meet this criterion. Quantitative analysis of the spatial variability of individual fracture and fracture network properties in existing and new data sets has the potential to reveal previously unknown patterns in the spatial variability of fracture networks. Only after documenting these patterns can we begin to understand and accurately model the underlying processes and properties that might exert spatially varying degrees of influence over fracture network evolution.

In this study we used the directional semivariogram to investigate the spatial variability of a fracture network developed in a map-scale anticline, near a kilometer-scale normal fault. We discovered that the amount of spatial variability in fracture intensity and intersection density increases toward the fault, and diminishes to what may be a background level at distances > 1–2 km from the fault. There is significant anisotropy in the spatial correlation structure of the overall fracture network variability, and this anisotropy is correlated to the trends of the anticline and fault. The direction of minimum spatial correlation is normal to the fault in areas close to it, and gradually rotates to be subparallel to the fold axis over the same 1–2 km distance away from the fault. We interpret these changes to reflect the varying scales of influence of the fault and the fold on fracture network property variability: the fold sets the background level and structure of variability, whereas the fault locally increases variability and alters its spatial correlation structure.

Stochastic modeling of fracture networks is widespread in fields related to groundwater, CO_2 sequestration, hydrocarbon production, and mining. Most of these models draw randomly from a known or presumed distribution of fracture properties like length, aperture and orientation. Fractures with these property distributions are then distributed through a model rock volume, often times according to a random function. The resulting spatial distribution of model fractures and fracture network properties is not routinely examined to ensure that it displays a structure that matches that of fracture networks in similar structural and stratigraphic settings. The directional semivariogram provides a means to do this, and its increased use should result in more accurate and reliable models.

Acknowledgements

excellent stewardship and guidance in their roles as editors.

Appendix A. Terminology, concepts, and principles in geostatistics

Understanding, adoption, and use of geostatistics and geostatistical tools by geologists have in part been hampered by terminology and misinterpretation of some foundational concepts and principles. During the review of this manuscript, the editors and one reviewer challenged us to concisely explain some confusing aspects of geostatistics so that more geoscientists might be encouraged to explore their application to geoscientific problems. Everyone recognized this as an important scientific goal that is not the purpose of this paper, and this Appendix is the result. We are by no means geostatistical experts, and caution readers that any concise summary of complex, nuanced topics will be incomplete, and therefore risks being simplified to the point of being inaccurate. We hope we have avoided this pitfall. Readers are encouraged to seek comprehensive explanations of the topics we briefly cover here, and excellent starting places include the geostatistical texts by Goovaerts (1997), Deutsch and Journel (1998), Isaaks and Srivastava (1989), Deutsch (2002), and Rubin (2003).

Geostatistics is a set of probabilistic tools for estimating the value of attribute z at unsampled locations described by the vector, $\mathbf{u}_\alpha$, where $\alpha = 1, \ldots, n$ denotes unique positions within study area A. This can be thought of, for example, as interpolation and extrapolation of porosity values in a reservoir with a limited set of porosity measurements that are distributed throughout it. To facilitate such estimations (i.e., predictions) it is useful to assume that the spatially referenced field data are the outcome of a *random process*. In this context the term *random* is invoked to acknowledge that we frequently lack complete knowledge of the numerous, complex, time- and scale-dependent natural processes responsible for any given measurement (Isaaks and Srivastava, 1989, p. 200–201). The fact that we make this assumption should not be taken to mean that the processes controlling porosity are random; this is simply a mathematical/statistical construct that allows us to begin to tackle the problem of predicting z at unsampled locations.

In geological systems, field sampling returns a set of n measurements of z acquired at locations $\mathbf{u}_\alpha$ within A, which is represented as a sampling distribution: $S_n = \{z(\mathbf{u}_\alpha), \alpha = 1, \ldots, n\}$. Here, it is mathematically/statistically convenient to consider that each $z(\mathbf{u}_\alpha)$ represents the outcome of a random process. The combination of all possible outcomes for the random process is called the regionalized variable (RV), which is denoted as $Z(\mathbf{u})$ (Deutsch, 2002, p. 102–105; Deutsch and Journel, 1998, p. 10–11; Goovaerts, 1997, p. 70–71). Perhaps the single most challenging aspect of the RV construct is to recognize that repetitive sampling of z at specific location $\mathbf{u}$ is required to estimate the cumulative distribution function (F) of $Z(\mathbf{u})$: $F(\mathbf{u}; z) = \text{Prob}\{Z(\mathbf{u}) \leq z\}$ (Goovaerts, 1997, p. 70–71; Deutsch, 2002, p. 102–105). As a result, geostatistical analysis makes the *a priori* assumption that measured (i.e., known) values of z at location $\mathbf{u}$ obviate the need to estimate $F(\mathbf{u}; z)$ because there is rarely more than one measured z for each location $\mathbf{u}$. In other words, a single measurement of porosity at location $\mathbf{u}$ represents one outcome of the function $F(\mathbf{u}; z)$, and there is rarely, if ever, more than one porosity measurement acquired from a specific location. Consequently, the requirement for repetitive sampling at a specific location, $\mathbf{u}$, is traded in favor of replicating z (e.g., porosity) at multiple, other locations, $\mathbf{u}_\alpha$, where $\mathbf{u} \neq \mathbf{u}_\alpha$ within A (Deutsch, 2002, p. 103). This leads to the overall paradigm underlying geostatistical inference: that $F(\mathbf{u}; z)$ can be estimated on the basis of the sampling distribution S_n. The decision to accept this trade in replication of z at a specific location, $\mathbf{u}$, for replication across the study area, A, is an intrinsic property of the RV construct, rather than a property of the underlying sampling distribution (i.e., the data). Deutsch (2002, p. 103), Deutsch and Journel (1998, p. 12), and Goovaerts (1997, p. 70–71) refer to this as the "decision of stationarity."

In practice, the decision of stationarity (often compactly referred to as simply, stationarity) is connected to the manner in which data are pooled for analysis (Deutsch and Journel, 1998, p. 12). For example, a geologist may be interested in the spatial variability of porosity within a sandstone reservoir, thus porosity would be the RV. As a result, geostatistical analysis of the porosity data intrinsically assumes that the RV exhibits stationarity, which is to say reservoir porosity results from *the same* physical and chemical processes. This may prove to be a poor decision if subsequent analyses or the addition of more data demonstrate that porosity exhibits a bimodal probability distribution. In this case, the bimodal distribution suggests that porosity is an outcome of multiple, *different* physical and chemical processes within the reservoir (e.g., sedimentation or compaction rates, sediment source(s), lithification processes, etc.). As a consequence, the choice to perform semivariogram analysis on the complete set of porosity data may yield misleading or inaccurate spatial correlation models. In contrast, the analyst may decide to segregate the porosity data into two smaller distributions, which could reveal that each sub-distribution is characterized by dramatically different spatial correlation structure. Within the RV construct, this latter example suggests that more than one RV is responsible for porosity within the reservoir, and each RV is likely to be governed by a unique combination of physical and chemical processes. Consequently, geologists are well served to recognize that decisions about how data are pooled for analysis are likely to impact the spatial correlation structure. This example is provided to illustrate several important aspects of stationarity: (1) the decision can be shown to be inappropriate when data are improperly pooled, e.g., semivariogram analysis of a bimodal distribution; (2) the decision may be revised and/or refined as additional data become available, e.g., subdividing data into smaller sub-distributions; and (3) stationarity is embedded into the choice of RV, and, as a result, stationarity is an intrinsic property of the RV that cannot be *a priori* proven correct (Deutsch and Journel, 1998, p. 12).

References

André-Mayer, A.S., Sausse, J., 2007. Thickness and spatial distribution of veins in a porphyry copper deposit, Rosia Poieni, Romania. J. Struct. Geol. 29 (10), 1695–1708.

Berg, S.S., Skar, T., 2005. Controls on damage zone asymmetry of a normal fault zone: outcrop analyses of a segment of the Moab fault, SE Utah. J. Struct. Geol. 27, 1803–1822.

Billaux, D., Chiles, J.P., Hestir, K., Long, J., 1989. Three-dimensional statistical modelling of a fractured rock mass—an example from the Fanay-Augères mine. In: International Journal of Rock Mechanics and Mining Sciences & Geomechanics Abstracts, vol. 26, 3. pp. 281–299.

Bisdom, K., Gauthier, B.D.M., Bertotti, G., Hardebol, N.J., 2014. Calibrating discrete fracture-network models with a carbonate three-dimensional outcrop fracture network: implications for naturally fractured reservoir modeling. AAPG Bull. 98 (7), 1351–1376.

Choi, J.-H., Edwards, P., Ko, K., Kim, Y.-S., 2016. Definition and classification of fault damage zones: a review and a new methodological approach. Earth Sci. Rev. 152, 70–87. http://dx.doi.org/10.1016/j.earscirev.2015.11.006.

Cilona, A., Aydin, A., Likerman, J., Parker, B., Cherry, J., 2016. Structural and statistical characterization of joints and multi-scale faults in an alternating sandstone and shale turbidite sequence at the Santa Susana Field Laboratory: implications for their effects on groundwater flow and contaminant transport. J. Struct. Geol. 85, 95–114.

Cruikshank, K.M., Aydin, A., 1995. Unweaving the joints in Entrada sandstone, Arches National Park, Utah, U.S.A. J. Struct. Geol. 17 (3), 409–421.

Cruikshank, K.M., Zhao, G., Johnson, A.M., 1991. Analysis of minor fractures associated with joints and faulted joints. J. Struct. Geol. 13 (8), 865–886.

Davatzes, N., Aydin, A., 2003. Overprinting faulting mechanisms in high porosity sandstones of SE Utah. J. Struct. Geol. 25, 1795–1813.

Deng, B., Liu, S., Jansa, L., Yong, S., Zhang, Z., 2013. Fractal analysis of veins in Permian carbonate rocks in the Lingtanchang anticline, western China. Geofluids. http://dx.doi.org/10.1111/gfl.12059.

Deutsch, C.V., 2002. Geostatistical Reservoir Modeling. Oxford University Press, New York.

Deutsch, C.V., Journel, A.G., 1998. Geostatistical Software Library and User's Guide.

Oxford University Press, New York.

Dewit, J., Huysmans, M., Muchez, P., Hunt, D.W., Thurmond, J.B., Vergés, J., Saura, E., Fernández, N., Romaire, I., Esestime, P., Swennen, R., 2012. Reservoir characteristics of fault-controlled hydrothermal dolomite bodies: ramales platform case study. Geological Society, London. Spec. Publ. 370 (1), 83–109.

Doelling, H.H., 2000. Geology of Arches National Park, Grand county, Utah. In: In: Sprinkel, D.A., Chidsey Jr.T.C., Anderson, P.B. (Eds.), Geology of Utah's Parks and Monuments 28. Utah Geol.ogical Assoc.iation Publication, pp. 11–36.

Doelling, H.H., Oviatt, C.G., Huntoon, P.W., 1988. Salt deformation in the paradox region. Utah Geol. Mineral Surv. Bull. 122.

Doelling, H.H., 1985. Geologic Map of Arches National Park and Vicinity, Grand County, Utah. Utah Geological and Mineral Survey Map, vol. 74 Utah Geological Survey.

Dowd, P.A., Xu, C., Mardia, K.V., Fowell, R.J., 2007. A comparison of methods for the stochastic simulation of rock fractures. Math. Geol. 39 (7), 697–714.

Dyer, J.R., 1988. Using joint interactions to estimate paleostress ratios. J. Struct. Geol. 10 (7), 685–699.

Dyer, J.R., 1983. Jointing in Sandstones, Arches National Park, Utah. Unpublished Ph.D. dissertation. Stanford University, California.

Eckert, A., Connolly, P., Liu, X., 2014. Large-scale mechanical buckle fold development and the initiation of tensile fractures. Geochem. Geophys. Geosyst. 15. http://dx.doi.org/10.1002/2014GC005502.

Fairley, J., 2016. Models and Modeling: an Introduction for Earth and Environmental Scientists. John Wiley & Sons.

Fischer, M.P., Polansky, A., 2006. Influence of flaws on joint spacing and saturation: results of one-dimensional mechanical modeling. J. Geophys. Res. Solid Earth 111, B07403. http://dx.doi.org/10.1029/2005JB004115.

Gervais, F., Gentier, S., Chiles, J.P., 1995. Geostatistical analysis and hierarchical modelling of a fracture network in a stratified rock mass. In: Conference on Fractured and Jointed Rock Masses. Lawrence Berkeley Laboratory Publication, Lake Tahoe, pp. 153–159.

Gillespie, P., Walsh, J., Watterson, J., Bonson, C., Manzocchi, T., 2001. Scaling relationships of joint and vein arrays from the Burren, Co. Clare, Ireland. J. Struct. Geol. 23 (2–3), 183–201.

Gillespie, P.A., Johnston, J.D., Loriga, M.A., McCaffrey, K.J.W., Walsh, J.J., Watterson, J., 1999. Influence of layering on vein systematics in line samples. Geological Society, London. Spec. Publ. 155 (1), 35–56.

Gillespie, P.A., Howard, C.B., Walsh, J.J., Watterson, J., 1993. Measurement and characterization of spatial distributions of fractures. Tectonophysics 226, 113–141.

Goovaerts, P., 1997. Geostatistics for Natural Resource Evaluation. Oxford University Press, New York.

Graham, J., 2004. Arches National Park Geologic Resource Evaluation Report. Natural Resource Report NPS/NRPC/GRD/NRR-2004/005. National Park Service, Denver, Colorado.

Gudmundsson, A., Berg, S.S., Lyslo, K.B., Skurtveit, E., 2001. Fracture networks and fluid transport in active fault zones. J. Struct. Geol. 23 (2), 343–353.

Guéguen, Y., Palciauskas, V., 1994. Introduction to the Physics of Rocks. Princeton University Press.

Han, W., Kim, K.-Y., Choung, S., Jeong, J., Jung, N.-H., Park, E., 2014. Non-parametric simulations-based conditional stochastic predictions of geologic heterogeneities and leakage potentials for hypothetical CO_2 sequestration sites. Environ. Earth Sci. http://dx.doi.org/10.1007/s12665-013-2653-z. Springer-Verlag Berlin Heidelberg.

Hanke, J.R., 2015. Quantifying the Spatial Variability of Fractures and Fracture Network Properties. unpublished MS thesis. Geology and Environmental Geosciences, Northern Illinois University, DeKalb, IL.

Hooker, J., Katz, R., 2015. Vein spacing in extending, layered rock: the effect of synkinematic cementation. Am. J. Sci. 315, 557–588.

Hooker, J., Laubach, S., Marret, R., 2013. Fracture-aperture size-frequency, spatial distribution, and growth processes in strata-bounded and non-strata-bounded fractures, Cambrian Mesón Group, NW Argentina. J. Struct. Geol. 54 54-51.

Hu, L.Y., Liu, Y., Scheepens, C., Shultz, A.W., Thompson, R.D., 2014. Multiple-point simulation with an existing reservoir model as training image. Math. Geosci. 46 (2), 227–240.

Huntoon, P., 1988. Late Cenozoic gravity tectonic deformation related to the paradox salts in the Canyonlands area of Utah. In: Doelling, H.H., Oviatt, C., Huntoon, P. (Eds.), Salt Deformation in the Paradox Region. Utah Geological & Mineral Survey, Salt Lake City, Utah, pp. 79–93.

Isaaks, E.H., Srivastava, R.M., 1989. Applied Geostatistics. Oxford University Press, New York.

Journel, A.G., 1996. Modelling uncertainty and spatial dependence: stochastic imaging. Int. J. Geogr. Inf. Syst. 10 (5), 517–522.

Journel, A.G., Huijbregts, Ch.J., 1978. Mining Geostatistics. Academic Press Inc.

Kitanidis, P., 1997. Introduction to Geostatistics: Applications in Hydrogeology. Cambridge University Press.

Koike, K., Kubo, T., Liu, C., Masoud, A., Amano, K., Kurihara, A., Matsuoka, T., Lanyon, B., 2015. 3D geostatistical modeling of fracture system in a granitic massif to characterize hydraulic properties and fracture distribution. Tectonophysics 660, 1–16.

Kupfersberger, H., Deutsch, C., 1999. Methodology for integrating analog geologic data in 3-D variogram modeling. AAPG Bull. 83 (8), 1262–1278.

La Pointe, P.R., Hudson, J.A., 1985. Characterization and interpretation of rock mass joint patterns. Geol. Soc. Am. Spec. Pap. 199, 1–38.

Laubach, S., Eichubl, P., Hargrove, P., Ellis, M.A., Hooker, J.N., 2014. Fault core and damage zone fracture attributes vary along strike owing to interaction of fracture growth, quartz accumulation, and differing sandstone composition. J. Struct. Geol. 68, 207–226.

Li, J.Z., Laubach, S.E., Gale, J.F.W., Marrett, R.A., 2017. Quantifying opening-mode fracture spatial organization in horizontal wellbore image logs, core and outcrop: application to upper cretaceous frontier formation tight gas sandstones, USA. J. Struct. Geol. http://dx.doi.org/10.1016/j.jsg.2017.07.005.

Liu, X., Eckert, A., Connolly, P., 2016. Stress evolution during 3D single-layer visco-elastic buckle folding: implications for the initiation of fractures. Tectonophysics 679, 140–155. http://dx.doi.org/10.1016/j.tecto.2016.04.042.

Long, J., Billaux, D.M., 1987. From field data to fracture network modeling: an example incorporating spatial structure. Water Resour. Res. 23 (7), 1201–1216.

Lorenz, J.C., Cooper, S.P., 2009. Extension-fracture patterns in sandstones above mobile salt: the Salt Valley anticline, Arches National Park, Utah. The Paradox Basin revisited-new developments in Petroleum systems and basin analysis. Rocky Mt. Assoc. Geol. Spec. Publ. 198–220.

Maerten, L., Gillespie, P., Pollard, D.D., 2002. Effects of local stress perturbation on secondary fault development. J. Struct. Geol. 24, 145–153.

Maerten, L., Maerten, F., 2006. Chronologic modeling of faulted and fractured reservoirs using geomechanically based restoration: technique and industry applications. Am. Assoc. Petrol. Geol. Bull. 90, 1201–1226.

Marrett, R.A., Gale, J.F.W., Gómez, L.A., Laubach, S.E., 2017. Correlation analysis of fracture arrangement in space. J. Struct. Geol. http://dx.doi.org/10.1016/j.jsg.2017.07.005.

Matheron, G., 1973. The intrinsic random functions and their applications. Adv. Appl. Probab. 5 (3), 439–468.

Matheron, G., 1963. Principles of geostatistics. Econ. Geol. 58, 1246–1266.

Miller, H.J., 2004. Tobler's first law and spatial analysis. Ann. Assoc. Am. Geogr. 94, 284–289.

Myers, D.E., 1989. To be or not to be… Stationary? That is the question. Math. Geol. 21 (3), 347–362.

Neuman, S.P., 2005. Trends, prospects and challenges in quantifying flow and transport through fractured rocks. Hydrogeol. J. 13 (1), 124–147.

Olson, J.E., 2004. Predicting fracture swarms—the influence of subcritical crack growth and the crack-tip process zone on joint spacing in rock. Geological Society, London. Spec. Publ. 231 (1), 73–88.

Ortega, O.J., Marrett, R.A., Laubach, S.E., 2006. A scale-independent approach to fracture intensity and average spacing measurement. AAPG Bull. 90 (2), 193–208.

O'Sullivan, D., Unwin, D., 2010. In: Hoboken, N.J. (Ed.), Geographic Information Analysis, second ed. John Wily & Sons.

Pollard, D.D., Fletcher, R.C., 2005. Fundamentals of Structural Geology. Cambridge University Press.

Pollyea, R.M., Fairley, J.P., Podgorney, R.K., McLing, T.L., 2013. A field sampling strategy for semivariogram inference of fractures in rock outcrops. Stoch. Environ. Res. Risk Assess. 27 (7), 1735–1740. http://dx.doi.org/10.1007/s00477-013-0710-5.

Pollyea, R.M., Fairley, J.P., 2012. Implications of spatial reservoir uncertainty for CO_2 sequestration in the east Snake River Plain, Idaho (USA). Hydrogeol. J. 20 (4), 689–699. http://dx.doi.org/10.1007/s10040-012-0847-1.

Pollyea, R.M., Fairley, J.P., 2011. Estimating surface roughness of terrestrial laser scan data using orthogonal distance regression. Geology 39 (7), 623–626. http://dx.doi.org/10.1130/G32078.1.

Putz-Perrier, M.W., Sanderson, D.J., 2010. Distribution of faults and extensional strain in fractured carbonates of the North Malta Graben. Am. Assoc. Petrol. Geol. Bull. 94 (4), 435–456. http://dx.doi.org/10.1306/08260909063.

Rafiee, A., Vinches, M., 2008. Application of geostatistical characteristics of rock mass fracture systems in 3D model generation. Int. J. Rock Mech. Min. Sci. 45 (4), 644–652.

Riley, P.R., Goodwin, L.B., Lewis, C.J., 2010. Controls on fault damage zone width, structure, and symmetry in the Bandelier Tuff, New Mexico. J. Struct. Geol. 32, 766–780. http://dx.doi.org/10.1016/j.jsg.2010.50.005.

Rohrbaugh Jr., M.B., Dunne, W.M., Mauldon, M., 2002. Estimating fracture intensity, density, and mean length using circular scan lines and windows. AAPG Bull. 86 (12), 2089–2104.

Rotevatn, A., Sandve, T.H., Keilegavlen, E., Kolyukhin, D., Fossen, H., 2013. Deformation bands and their impact on fluid flow in sandstone reservoirs: the role of natural thickness variations. Geofluids 13 (3), 359–371.

Rubin, Y., 2003. Applied Stochastic Hydrogeology. Oxford University Press.

Sagi, D.A., De Paola, N., McCaffrey, K.J.W., Holdsworth, R.E., 2016. Fault and fracture patterns in low porosity chalk and their potential influence on sub-surface fluid flow—a case study from Flamborough Head, UK. Tectonophysics 690, 35–51.

Sanderson, D.J., Nixon, C.W., 2015. The use of topology in fracture network characterization. J. Struct. Geol. 72, 55–66.

Santos, R.F., Miranda, T.S., Barbosa, J.A., Gomes, I.F., Matos, G.C., Gale, J.F., Neumann, V.H., Guimarães, L.J., 2015. Characterization of natural fracture systems: analysis of uncertainty effects in linear scanline results. AAPG Bull. 99 (12), 2203–2219.

Savage, H.M., Brodsky, E.E., 2011. Collateral damage: evolution with displacement of fracture distribution and secondary fault strands in fault damage zones. J. Geophys. Res. 116, B03405. http://dx.doi.org/10.1029/2010JB007665.

Şen, Z., 2009. Spatial Modeling Principles in Earth Sciences. Springer, Netherlands.

Sisavath, S., Mourzenko, V., Genthon, P., Thovert, J.F., Adler, P.M., 2004. Geometry, percolation and transport properties of fracture networks derived from line data. Geophys. J. Int. 157 (2), 917–934.

Soden, A.M., Lunn, R.J., Shipton, Z.K., 2016. Impact of mechanical heterogeneity on joint

density in a welded ignimbrite. J. Struct. Geol. 89, 118–129.

Stein, M.L., 2012. Interpolation of Spatial Data: Some Theory for Kriging. Springer Science + Business Media, New York.

Tobler, W.R., 1970. A computer movie simulating urban growth in the Detroit region. Econ. Geogr. 46, 234–240.

Trudgill, B.D., 2011. Evolution of salt structures in the northern Paradox Basin: controls on evaporite deposition, salt wall growth and supra-salt stratigraphic architecture. Basin Res. 23 (2), 208–238.

Viruete, J., Carbonell, R., Marti, Pérez-Estaún, A., 2003. 3-D stochastic modeling and simulation of fault zones in the Albalá granitic pluton, SW Iberian Variscan Massif. J. Struct. Geol. 25, 1487–1506.

Watkins, H., Bond, C.E., Healy, D., Butler, R.W., 2015. Appraisal of fracture sampling methods and a new workflow to characterise heterogeneous fracture networks at outcrop. J. Struct. Geol. 72, 67–82.

Webster, R., Oliver, M., 1992. Sample adequately to estimate variograms of soil properties. J. Soil Sci. 43, 177–192.

Wennberg, O.P., Casini, G., Jonoud, S., Peacock, D.C.P., 2016. The characteristics of open fractures in carbonate reservoirs and their impact on fluid flow: a discussion. Pet. Geosci. http://dx.doi.org/10.1144/petgeo2015-003.

Zamanian, S., Fehler, M., Fang, X., Burns, D., 2014. A Bayesian framework for fracture characterization from surface seismic data. Geophys. J. Int. 199, 1230–1244.

Zhao, G., Johnson, A.M., 1992. Sequence of deformations recorded in joints and faults, Arches National Park, Utah. J. Struct. Geol. 14 (2), 225–236.